AUTOROTATION OF THIN PLATES

by

FABIAN ANDERSEN

B.Sc., University of Alberta, 1965

A THESIS SUBMITTED IN PARTIAL FULFILLMENT OF

THE REQUIREMENTS FOR THE DEGREE OF

M.A.Sc.

in the Department

of

Mechanical Engineering

We accept this thesis as conforming to the

required standard

THE UNIVERSITY OF BRITISH COLUMBIA

March, 1970

In presenting this thesis in partial fulfilment of the requirements for an advanced degree at the University of British Columbia, I agree that the Library shall make it freely available for reference and study. I further agree tha permission for extensive copying of this thesis for scholarly purposes may be granted by the Head of my Department or by his representatives. It is understood that copying or publication of this thesis for financial gain shall not be allowed without my written permission.

Department of Mechanical Engineering

The University of British Columbia
Vancouver 8, Canada

Date 25 March 1970

ABSTRACT

A visualization technique is applied to the unsteady separated flow about an autorotating flat plate. An unsteady potential model is attempted to predict the pressure loading on the plate as a function of angle of attack.

To visualize the flow, a streakline is marked by low density air created by the wake of a heated wire probe. An off-center parabolic mirror Schlieren system detects the density gradient. Due to the highly unsteady nature (in this project, the plate rotates at almost 1,000 r.p.m. for a 10-foot per second freestream velocity) of the flow, high-speed 35mm. single lens reflex shots or 16mm. movie films recorded the image.

Timing marks on the movie film provided information of the angular speed of the plate during acceleration to the autorotation speed and at autorotation.

The two-dimensional unsteady attached flow model attempts to duplicate the effects of separation by superimposing vortices in the wake, as shown in the flow visualization, and by eliminating terms representing the freestream velocity in the range of 60 to 150 degrees angle of attack.

TABLE OF CONTENTS

FIGURES

ACKNOWLEDGEMENTS

The author wishes to express gratitude to Professor G. V. Parkinson for his assistance and optimism, particularly during the theoretical side of this project. The suggestions of Professor Z. Rotem concerning the Schlieren apparatus and photography saved many confused hours.

Thanks are due Mr. P. Hurren and Mr. J. Hoar, Chief Technicians, their staff and my fellow graduate students for helping to provide the hardware and for the aid in getting through the maze.

Special thanks to my wife, Cherie, for typing and for playing the role of a student's wife so well.

SYMBOLS

a	Ellipse major semi-axis	
b	Ellipse minor semi-axis	
d	Probe diameter	
B	Analytic function	
C	Chord of theoretical model	4 units
C_e	Chord of experimental plate	1 5/16"
C_p	Pressure coefficient	
C_D	Drag coefficient	
C_L	Lift coefficient	
C_T	Torque coefficient	
$F(z)$	Complex potential	
$W(z)$	Complex velocity	
n	Direction normal to surface	
s	Direction tangent to surface	
V_n	Normal velocity	
V_t	Tip velocity	
U	Freestream velocity	
p	Pressure	
$se^{i\delta}$	Vortex position in ζ plane	
$re^{i\phi}$	Point in ζ plane	
$Re^{i\theta}$	Point in z plane	
N_r	Reynolds no.	
G_r	Grashof no.	
t	Time	
z	Physical plane	
z'	Physical plane fixed with respect to rotating translating cylinder	

α	Angle of attack
α_o	Relative zero angle of attack
ϵ	Eliminator factor
ψ	Stream function
Φ	Velocity potential
ζ	Unit circle plane and a point in that plane
γ	The unit circle in ζ
σ	A point on γ
λ	Constant = (a-b)/(a+b)
w	Constant = (a+b)/2
Γ	Circulation per unit span
ρ	Mass density
ν	Viscosity
ω	Angular velocity
ω_a	Angular velocity at autorotation

I. INTRODUCTION

The type of autorotation investigated in this project is that which occurs when a flat plate, free to rotate about a spanwise mid-chord axis and in the presence of a uniform freestream perpendicular to the axis of rotation (Fig. 1), is given an initial angular velocity above a minimum in either direction. The plate then undergoes an angular acceleration up to a stable angular velocity known as the autorotational speed. At autorotation then the flow pattern is repeated every half revolution. Circulation is produced, giving a net positive lift for every cycle or one-half revolution.

Recently, Cheng (1) measured the instantaneous pressure at taps on the center line chord of the plate as a function of angle of attack. Using a mutual inductance transducer, he also measured the angular velocity and acceleration during the period of acceleration up to autorotation and at autorotational speed. Previously, Crabtree (2) and Neumark (3) reviewed and explored the possibilities of employing autorotating or powered (higher angular speeds) plates as lift producing devices in themselves or as lift augmenting and control devices replacing the flap on a conventional airfoil. In normal operation, the rotating flap not only produces lift but augments the circulation about the airfoil. Rotated backwards, it acts as a spoiler. When not in use, the flap can be aligned with the flow to give a low drag.

Crabtree and Neumark model the rotating flap on a conventional airfoil with a vortex acting upon a thin airfoil in potential flow. The vortex assumption may be valid for a powered rotating flap, since at higher angular velocities the flow is probably similar to that produced by a rotating circular cylinder, but the flow about an autorotating flap is highly unsteady.

James and Stone (7) measured the forces and angular velocities

of autorotating plates of various aspect ratios using a contact switch to record times at each half revolution and a three component balance. They also made an attempt to visualize the flow using fumes of titanium tetrachloride with the plate at autorotational speed, and recording the results by means of a camera and an electronic flash. The visualization gave some indication of the flow pattern close to the plate, but the fumes appear to diffuse too quickly to give an indication of downstream development. Similarly, Baird and Pick (8) measured the autorotational speed as a function of freestream velocity and aspect ratio.

This project includes:

i) Flow visualization during the acceleration period and at autorotation. The technique involved a Schlieren system, a heated wire probe and high-speed photography.

ii) Angular velocity-time and tip velocity-freestream velocity curves from timing pulses on the movie film.

iii) An unsteady attached flow two-dimensional potential model for this unsteady separated flow.

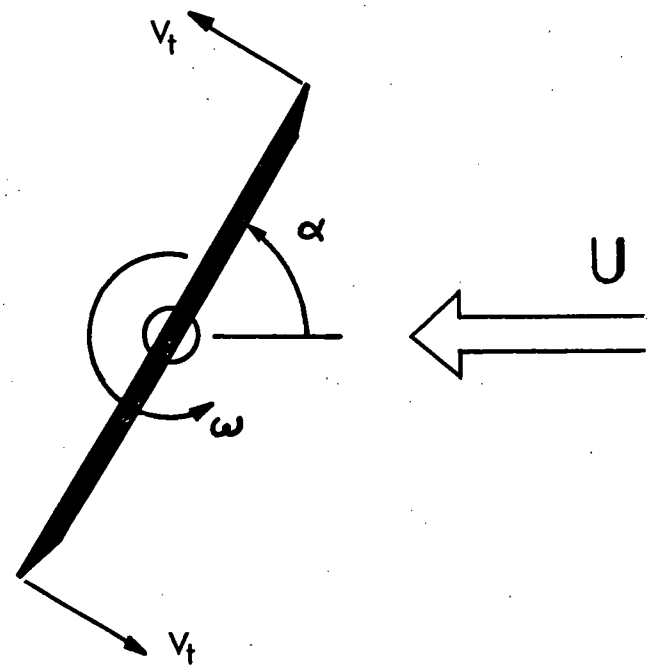

FIG. 1 PLATE ARRANGEMENT AND SYMBOLS

II. EXPERIMENTAL APPARATUS AND PROCEDURES

2.1 GENERAL OUTLINE

The visualization technique, in brief, consisted of a semi-focusing Schlieren system to render visible a hot streakline behind a probe upstream of an autorotating flat plate in a wind tunnel. Due to the highly unsteady nature of the flow, high-speed photography was employed to record the results.

2.2 WIND TUNNEL AND FLAT PLATE

An aluminum flat plate (Figs. 2-3) was mounted in an open circuit wind tunnel (top speed approximately 20 feet per second) with a 6"x12" working section. The flat plate was 6 inches long to span the width of the tunnel and 1 5/16" chord to give approximately the same blockage ratio (chord/height of working section) as Cheng (1).

The side walls of the tunnel were polished flat plate glass (to minimize optical aberration) and diamond drilled to accept the bearings (Fig. 2) for the plate.

The magnitude of the uniform freestream was measured with a pitot-static tube which was calibrated in a 36"x27" wind tunnel instrumented with a Betz manometer accurate to .02 millimeters of water.

2.3 SCHLIEREN SYSTEM AND HEATED-WIRE PROBE

The Schlieren system employed was the one used by Claassen (4). In brief, it is a semi-focusing (implying a source slit) off-center system (Figs. 4-5) employing 8-inch diameter parabolic mirrors of focal length 63.5 inches. Due to the short exposure times required, it was decided to take black and white pictures instead of colour to take advantage of the higher film speeds available. Thus, a horizontal knife edge was substituted for the colour filter used by Claassen.

A heated .010-inch Nichrome-V circular cross-section wire (Figs. 2-3) approximately one plate chord in length and one and a half plate chords upstream and on the same horizontal plane as the rotational axis illuminated a streakline. The length of wire was limited by oscillations and the one chord length was settled upon. A smaller diameter (.002") wire was tried, but this limited the heat output and the quality of the picture decreased.

The center line of the plate was aligned with the center line of the Schlieren system by using a one milliwatt laser as described by Claassen (4).

The effect of the buoyancy of the heated streakline is discussed in the appendix.

The supports for the probe were #20 solid core copper wire. Holes were drilled in the copper wire with a #80 twist drill and the Nichrome wire was soldered in place.

Originally, the power supply for the Schlieren tungsten light source was 110v 60-cycle. Since pictures were being taken at a top rate of 2,000 per second, the power supply caused overexposed frames at 120 cycles per second. Consequently, the power supply was altered to a variable amplitude 60-cycle source feeding into a full wave rectifier with 9,000 microfarads across the line.

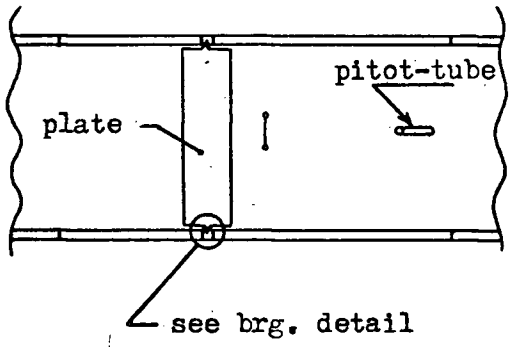

plan x-section

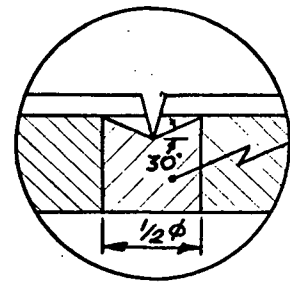

BEARING DETAIL

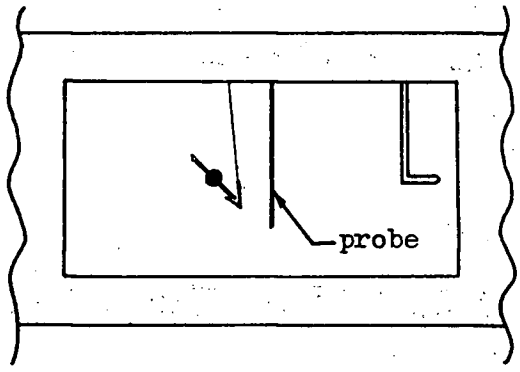

side view

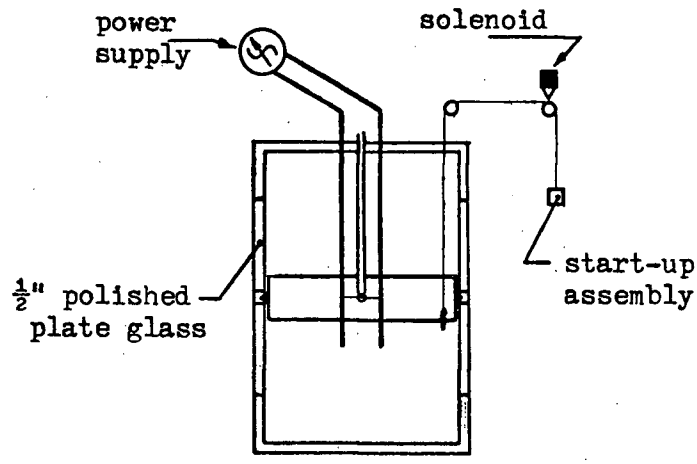

front x-section

NOTE: NOT TO SCALE

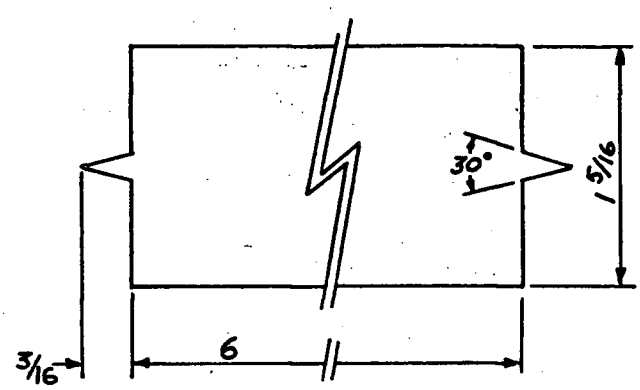

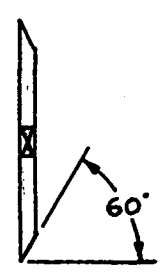

MAT'L: .050" aluminum

PLATE DETAIL

FIG. 2 WIND TUNNEL WORKING-SECTION SCHEMATIC

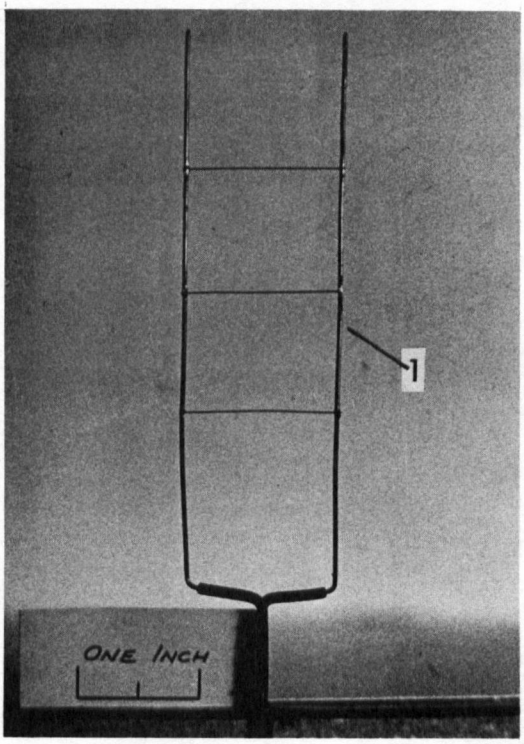

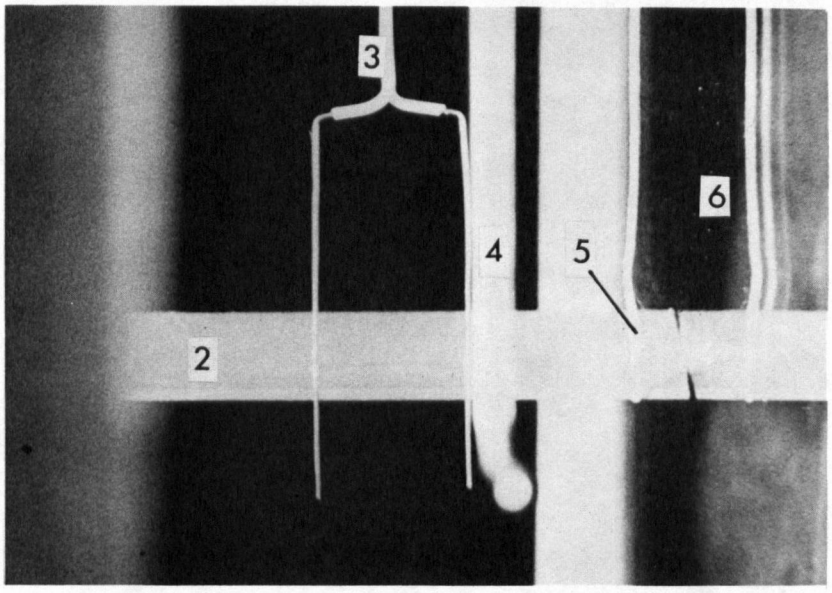

1. .010" diameter Nichrome V three wire probe
2. plate
3. .010" diameter Nichrome V single wire probe
4. pitot-static tube
5. starting hook
6. ½" plate glass and reflection

FIG. 3 WIND TUNNEL WORKING-SECTION ARRANGEMENT

2.4 HIGH-SPEED PHOTOGRAPHY

Two cameras were used to record the Schlieren image.

To record the entire image, a 35mm. Pentax Spotmatic S.L.R. camera body was used with a three wire probe (Fig. 3). The film was TRI-X taken at 1/1,000 seconds at a rated 400 ASA. Pictures were taken at random with the plate autorotating at a freestream velocity of 11.3 feet per second.

To obtain a continuous record of the plate accelerating from the initial angular velocity up to autorotational speed and also at autorotational speed, a 16mm. rotating prism high-speed camera body was used (brand name HYCAM) with a single wire probe. When the camera is started, the motor accelerates the film from the supply reel (100-foot capacity) to a take-up reel up to a predetermined speed (controlled by the camera power supply). The rotating prism moves the image at film speed during the exposure time (1/2.5 x 1/frames per second = exposure time).

The film used was Eastman 4-X (ASA 400) type 7224 double perforation negative pan.

To give the plate a controllable initial velocity and synchronize this with camera start-up, a solenoid, which was triggered by a microswitch in the HYCAM, released a weight attached to a hook (Figs. 2-3) to initiate autorotation. The HYCAM's microswitch closed after a set number of feet of film had left the supply reel.

2.5 PROCEDURE

i) The procedure for taking 35mm. random 'still' shots was as follows.

a) A three wire probe was placed one and a half chord lengths upstream of the plate axis with the middle wire on the horizontal plane of the axis of rotation. The pitot-static tube was lowered into place and the wind tunnel speed was set at 11.3 feet per second. A reference line was stretched parallel to the wind direction and through the axis of rotation to give a free-stream reference in the picture. Lights other than the Schlieren source were turned out. The probe power supply was then turned on until the wire reached a very dim red in colour (experience indicated that a bright red probe did not last very long).

b) The 35mm. Pentax Spotmatic camera body was set such that the image cast by the objective lens was in focus. The horizontal knife edge was raised or lowered to give a light gray background with good detail on the streak-line about the stationary plate. The proper exposure, as indicated on the Pentax averaged-through-the-lens light meter, was obtained by adjusting the light source power supply.

c) The tunnel speed was then given a final check and the pitot-static tube raised. Autorotation was initiated by releasing the starting weight.

d) Pictures were then taken at random with the plate at autorotation speed and the three wire probe in place.

ii) The procedure for taking high-speed movie films of the plate accelerating from rest was as follows.

a) A single wire probe was placed one and a half chord lengths upstream of the plate axis with the wire on the same horizontal plane as the rotational axis. The starting hook was then attached to the plate and a predetermined weight (one which would just initiate autorotation at that tunnel speed) added. The pitot-static tube was lowered and the tunnel speed set at either 11.3, 15.3 or 19.2 feet per second. A reference line was stretched parallel to the freestream direction and through the axis of rotation. Lights other than the Schlieren source were turned off. The probe power supply was then turned on and adjusted to give the probe a dim red colour.

b) The 16mm. 'HYCAM' camera body, with film threaded from supply to take-up reel, was set such that the image cast by the objective lens was in focus on the film in the gate. The camera cross hair was lined up with the reference line and the line removed. The A.C. solenoid from the start-up mechanism was then connected to the camera microswitch through a 6V A.C. power supply. To set the exposure, the light source power supply was adjusted by experience, since the 'HYCAM' exposure meter could not physically be used.

For acceleration shots, the camera gear box was set in low and the camera A.C. power supply set to take 300 p.p.s. (see Ref. 5). The camera timing light was set to 1,000 pulses per second.

c) The camera was then started by turning on the power supply. When a predetermined (selection on the camera) length of film (approximately 20 feet) had left the supply reel, the solenoid closed, triggering the plate to accelerate to autorotational speed.

d) The procedure for taking a film when the plate was at autorotational speed was similar except that the plate was autorotating when the camera was started. Also, the camera gear box was in high and the power supply adjusted (see Ref. 5) to give 2,000 p.p.s.

Generally, better results were obtained if the movie films were run at night. It is believed that this was due to a decrease in outside disturbances which vibrated the knife edge to give varying exposures throughout the film.

Films were analyzed for angle of attack-time relationships by mounting a fabricated plexiglass gate on a Leitz slide projector with supply and take-up reels from an editor. To prevent damage to the film from heat, an orange filter was placed between the light source and the film. Thus, it was possible to see four or five frames complete with timing marks at one time and it was convenient to handle the 100-foot lengths of film. The angles and time were tediously measured with protractor and ruler on the projected image.

All data was reduced on a digital computer.

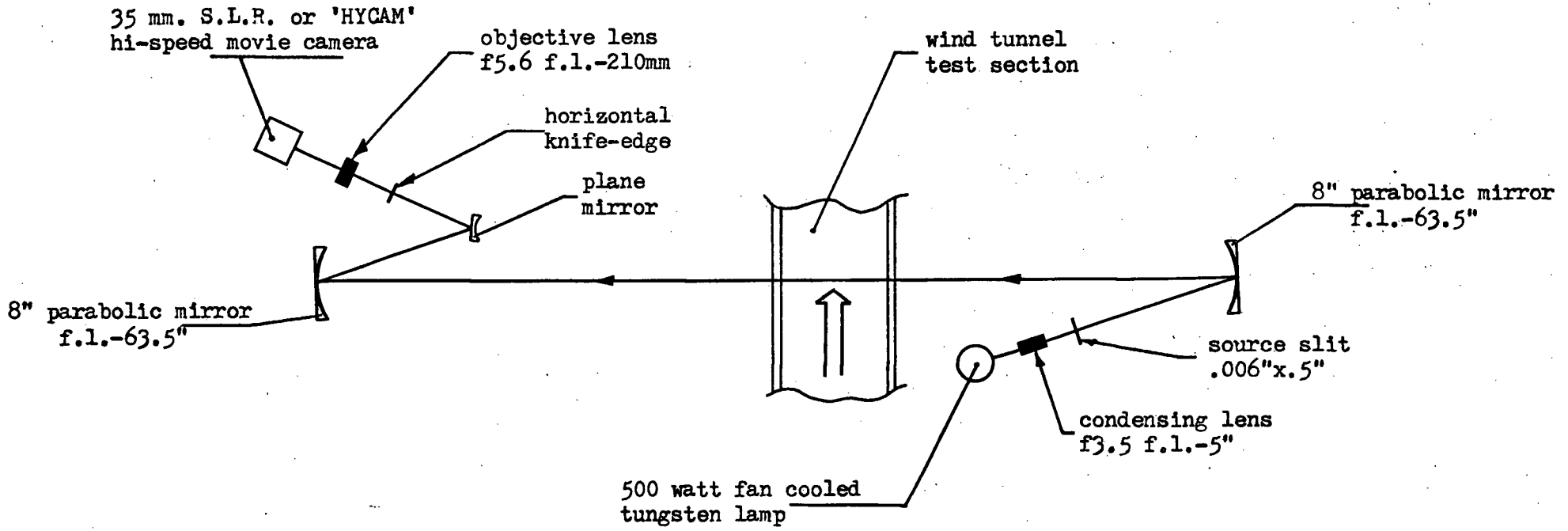

FIG. 4 SCHLIEREN - WIND TUNNEL WORKING-SECTION SCHEMATIC

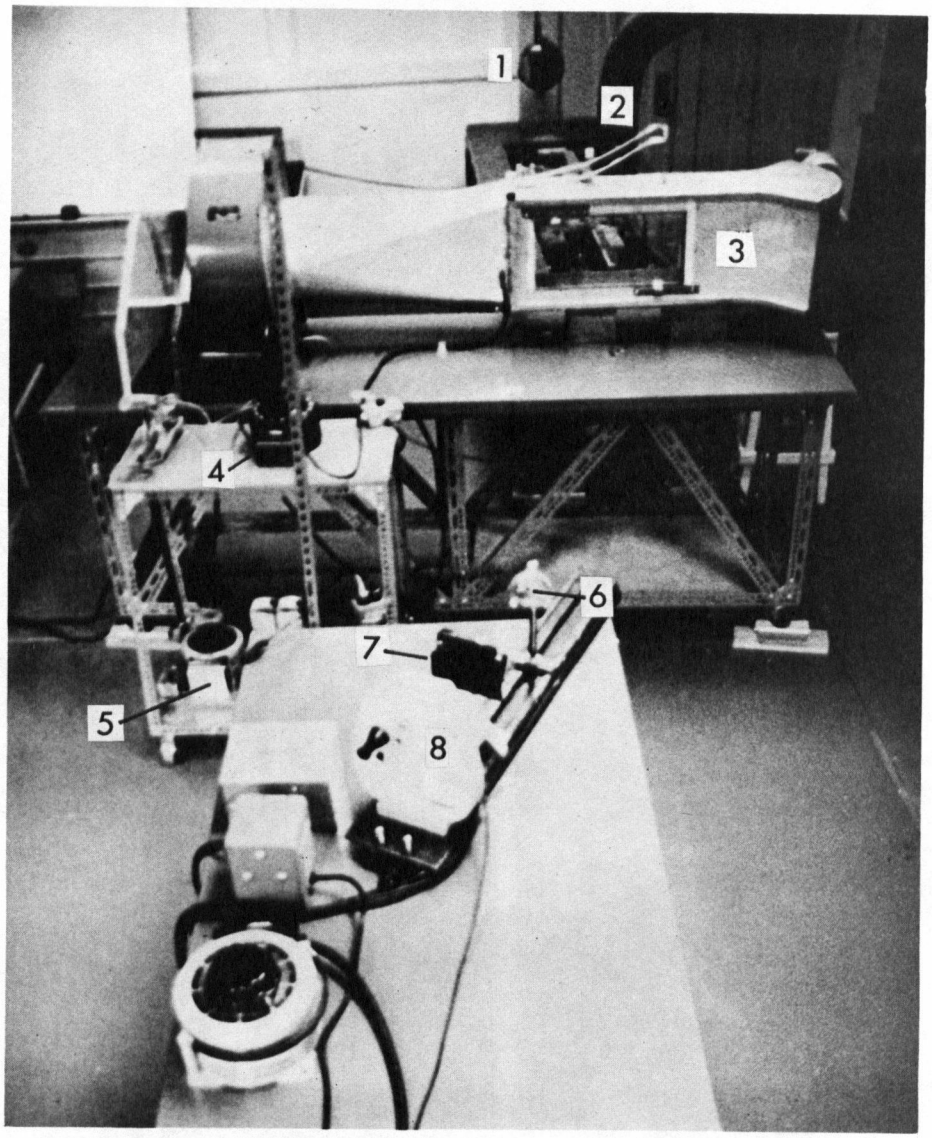

1. 8" diameter parabolic mirror
2. tungsten light source and cooling tube
3. wind tunnel
4. probe power supply
5. tungsten source power supply
6. plane mirror
7. knife-edge and objective lens
8. 'HYCAM' hi-speed camera body

FIG. 5 SCHLIEREN-WIND TUNNEL WORKING-SECTION ARRANGEMENT

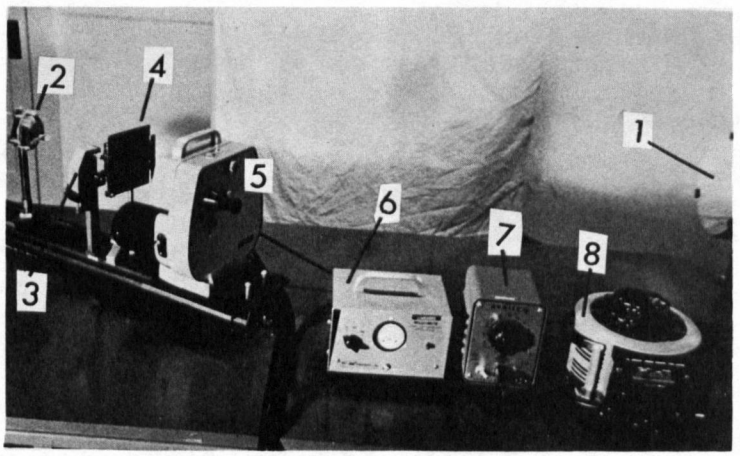

1. 8" diameter parabolic mirror
2. plane mirror
3. horizontal knife-edge
4. objective lens f5.6 f.l.-210mm
5. 'HYCAM' hi-speed camera body
6. timing light pulse generator
7. plate start-up solenoid power supply
8. camera power supply

FIG. 6 'HYCAM' HIGH-SPEED CAMERA

III. EXPERIMENTAL RESULTS

The results obtained from the visualization technique were 35mm. still photographs of the entire 8-inch diameter Schlieren field with three streaklines illuminated and 16mm. high-speed movie close-up films of the plate accelerating and at autorotational speed with one streakline illuminated. Velocity-time curves and tip velocity-freestream velocity curves were obtained from the movie films by measuring plate angles and time from 1/1,000 second timing marks on the edge of the film.

The sequence (Figs. 8-11) of random 35mm. shots at U = 11.3 feet per second show the flow field developing through one cycle, that is from zero to 180 degrees angle of attack. Flow is from the right parallel to the reference line and the plate is rotating anti-clockwise, as depicted in figure 7. Separation is delayed until the plate reaches a positive angle of attack close to the relative zero angle of attack (α_o see figure 7), due to the effect of the tip velocity. From the velocity curves, as will be discussed later, α_o = 34 degrees for U = 11.3 feet per second. A separation bubble begins to form at approximately 30 degrees angle of attack on the upstream tip. It grows in size, appears to develop into a vortex at about 45 degrees, then starts to shed radially outwards as the plate passes 90 degrees. By 120 degrees, the tip is beginning to pass this vortex. The influence of this vortex can be seen by comparing the flow pattern with Cheng's measured pressure coefficients (Figs. 25-30), particularly for angles of attack of 60 and 90 degrees. It is seen that the largest suction peaks measured during

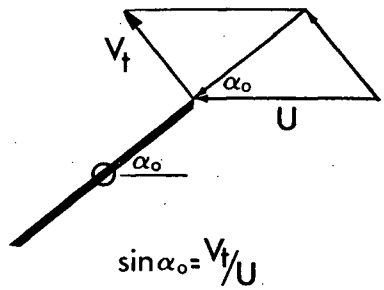

FIG. 7

the complete cycle occur near the position of this 'dominant' vortex.

This vortex continues to influence the flow pattern near the plate during the next cycle as another vortex is formed at this tip. It moves downstream and is deflected downwards by the generated circulation. The deflection of the wake can best be seen by noting that the position of the lower streakline for all angles of attack is lower than at the marking point. The wake is deflected in the same direction as the plate rotation irrespective of the angle of attack.

Not so visible is a vortex forming at the other tip and becoming visible as the plate approaches 90 degrees. It appears to start shedding at near 120 degrees as the tip moves upstream. An unstable shear layer trailing this vortex forms at this tip until a positive angle of attack is reached where the 'dominant' vortex forms. Again, Cheng measured relatively high suctions (Figs. 25-30) near this vortex.

The plate appears bent in the 35mm. pictures near the zero and 180 degree angles of attack, since the S.L.R. has a focal plane shutter which allows a discrete time difference as the exposure slit travels from the left of the image to the right.

The movie films of the plate accelerating from rest are too lengthy to reproduce here, since the acceleration period is in the order of five seconds and 300 p.p.s. were taken. The initial angular velocity appears to delay separation at small positive angles of attack, thus setting up the autorotation flow pattern. As the plate accelerates, the angle of relative zero angle of attack increases until the autorotation speed is reached.

Enlargements of 16mm. frames at angles of attack closest to 15 degree intervals from zero to 180 degrees are shown in figures 12-15 with the plate at autorotational speed and the freestream at 11.3 feet per second. Only twelve frames of approximately sixty for one cycle are shown. These pictures

show a limited part of the Schlieren field to give a better indication of the flow development near the plate. Separation at the upstream tip begins to occur at an angle of approximately 28 degrees. A separation bubble forms and the 'dominant' vortex is formed and shed, as described before. Here the vortex at the other tip becomes visible at about 75 degrees and appears to shed with the development of a shear layer feeding into it.

Velocity-time (Figs. 16-18) and tip-freestream velocity (Figs. 19-20) curves were obtained from measurements of angles and times on both the acceleration and at-speed movie films. It is seen that even though the difference between final tip speed and the initial tip velocity is greatest for the highest freestream velocity, the time taken to reach autorotational speed is lowest for the highest freestream velocity. That is, for the range investigated, the higher the freestream velocity the lower (considering minimum start-up velocity runs) the acceleration period. This is in agreement with Cheng's (1) results.

Within the error involved in measuring angles and times from the films, the angular velocity was constant during a cycle at autorotation.

The tip velocity varies linearly with the freestream velocity and the equation of the curve is

$$V_T = .814U - 2.84$$

This result is compared to Cheng's in figure 20. The linear portion of Cheng's curve for the case using end plates is given by

$$V_T = .65U - 3.74$$

Cheng's model had a larger thickness ratio (4.7%) and a smaller aspect ratio (3.0) than the plate in this project (3.8% and 4.5). In this project, the minimum initial velocity required to start autorotation would appear to increase slightly with freestream velocity. Cheng's results showed the opposite trend and this velocity is most probably a function of the type of bearings used.

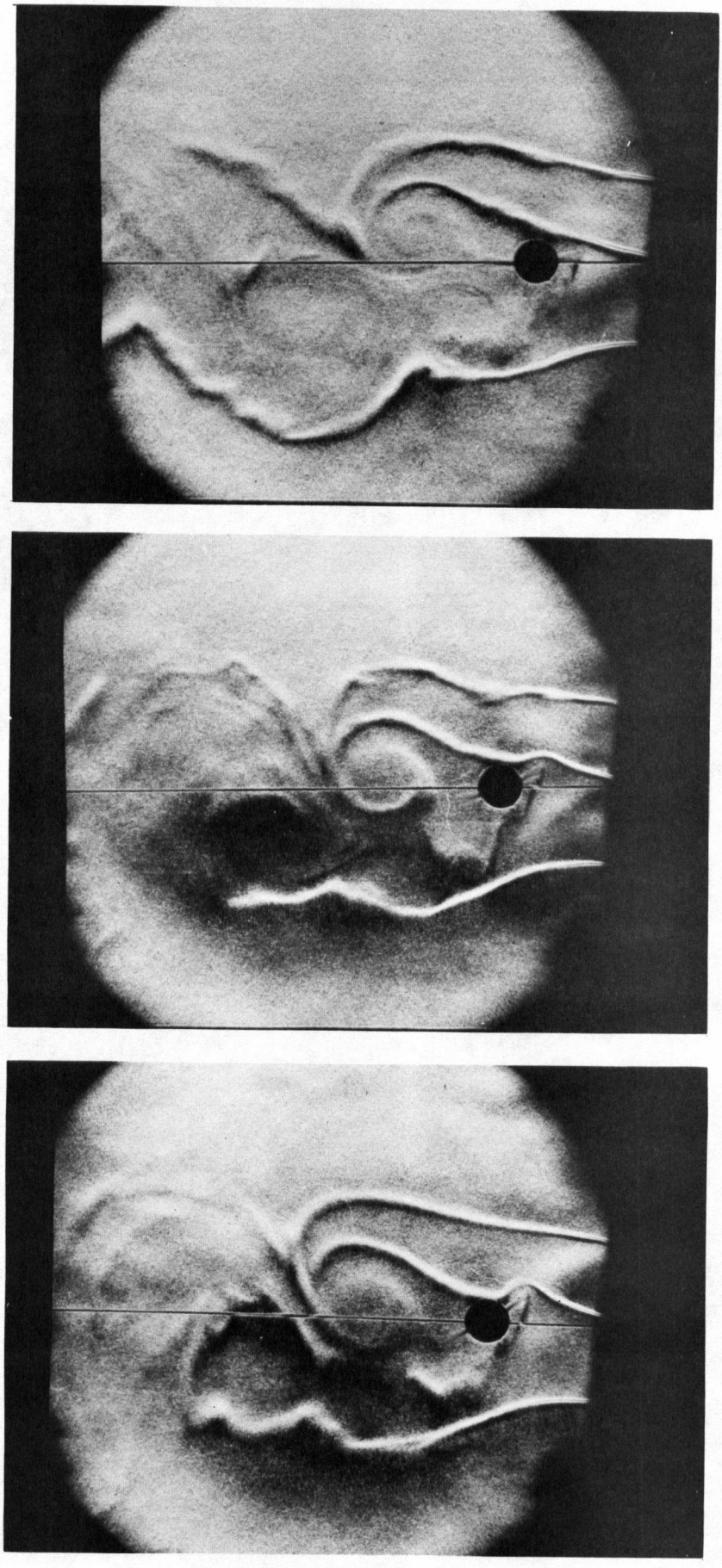

FIG. 8 35mm. RANDOM PICTURES
U = 11.3 ft./sec.

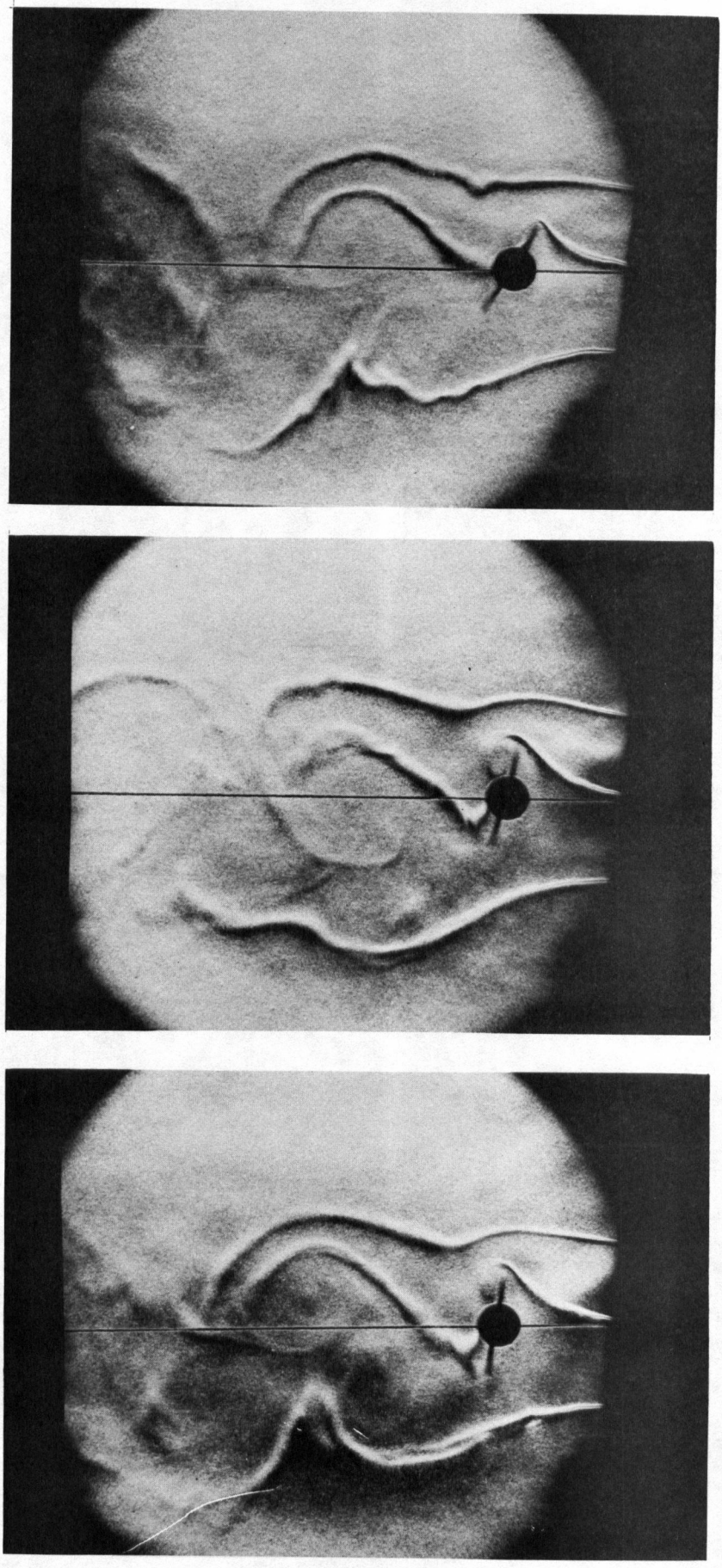

FIG. 9 35mm. RANDOM PICTURES
U = 11.3 ft./sec.

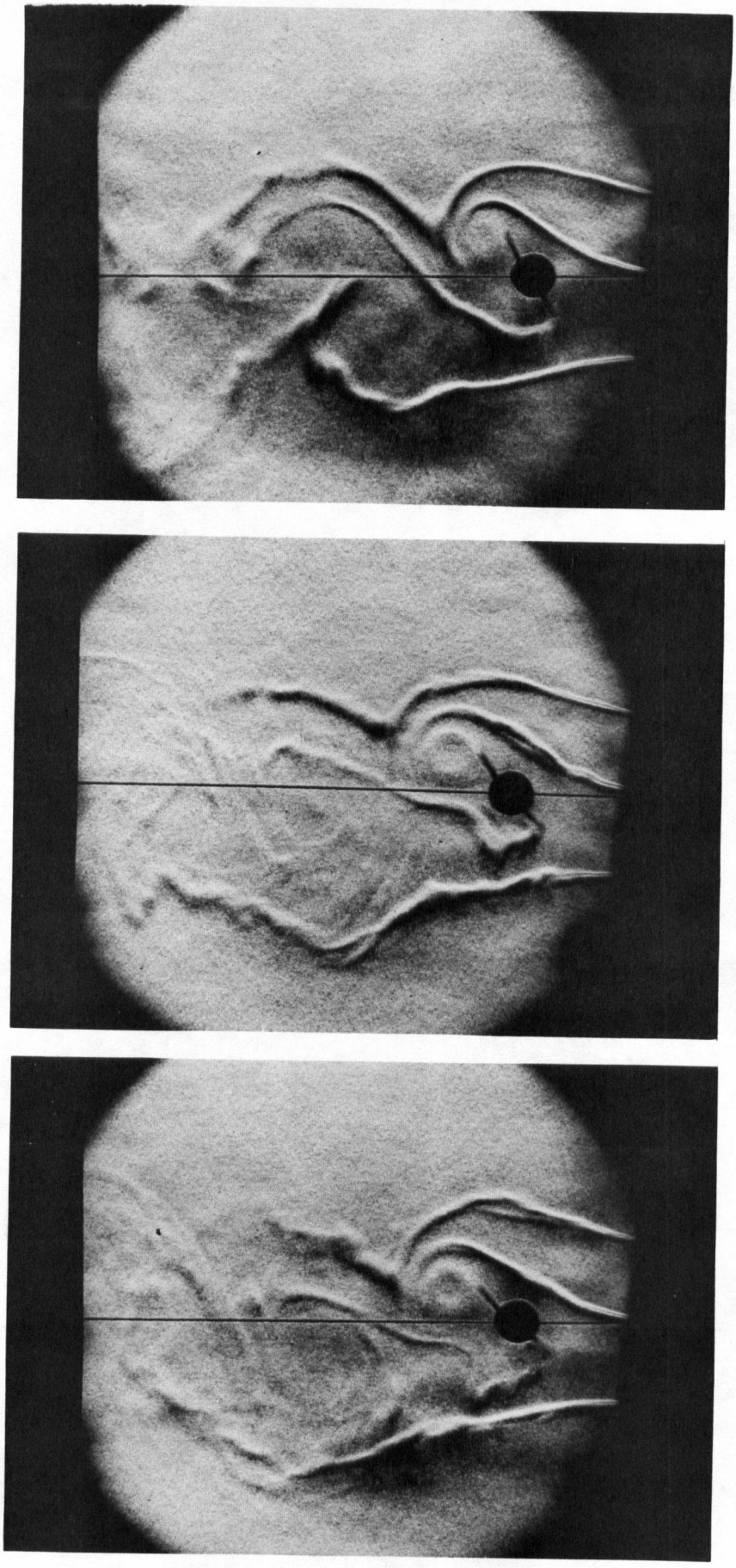

FIG 10 35mm RANDOM PICTURES
U=11.3 ft./sec

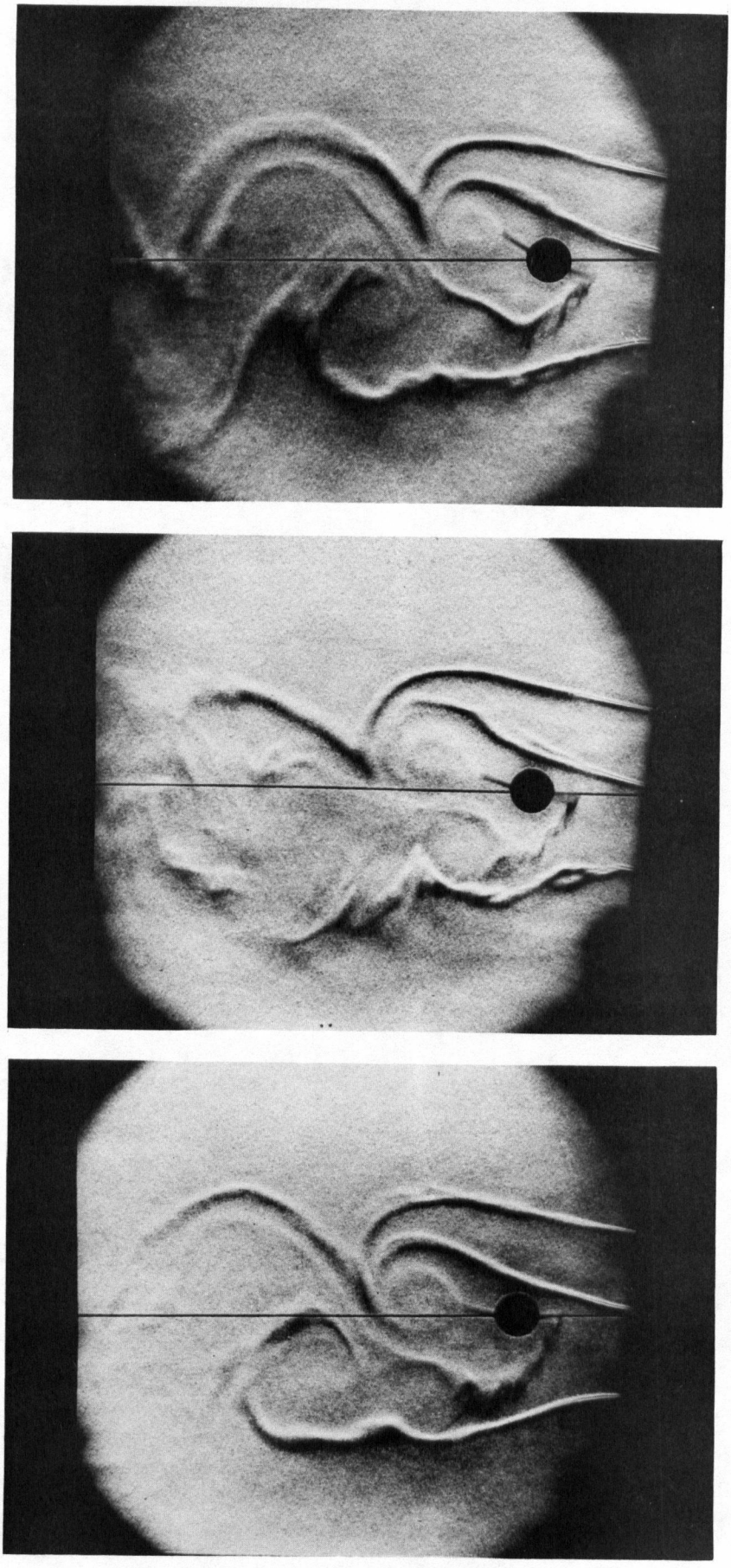

FIG. 11 35mm. RANDOM PICTURES
U = 11.3 ft./sec.

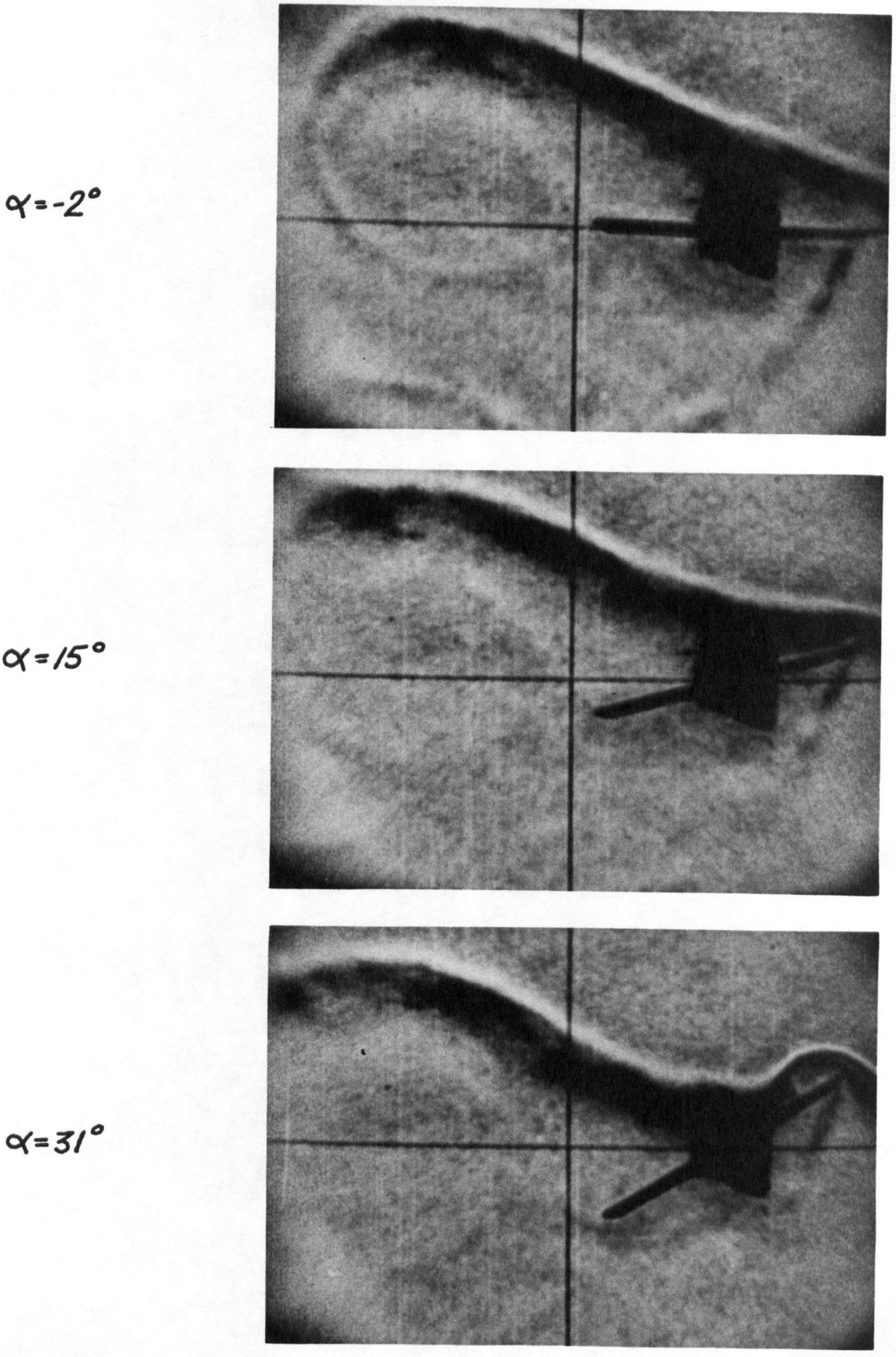

FIG. 12 16mm. MOVIE FILM FRAMES
U = 11.3 ft./sec.

$\alpha = 44°$

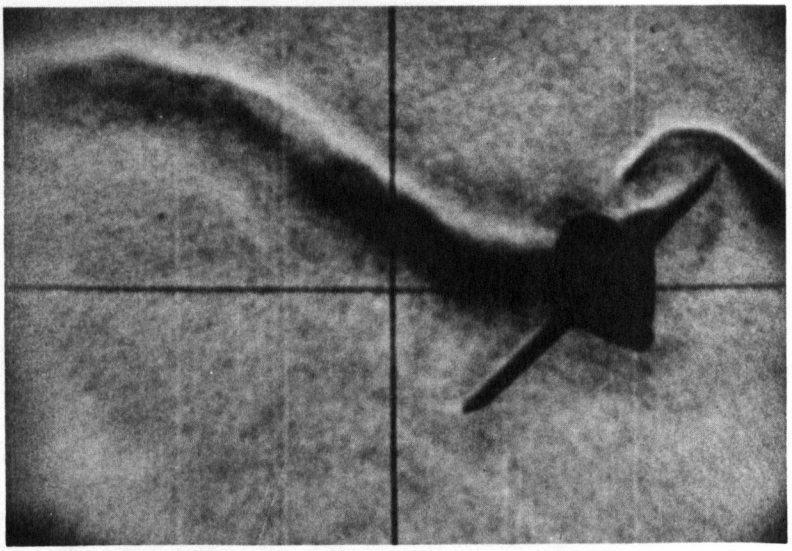

$\alpha = 60°$

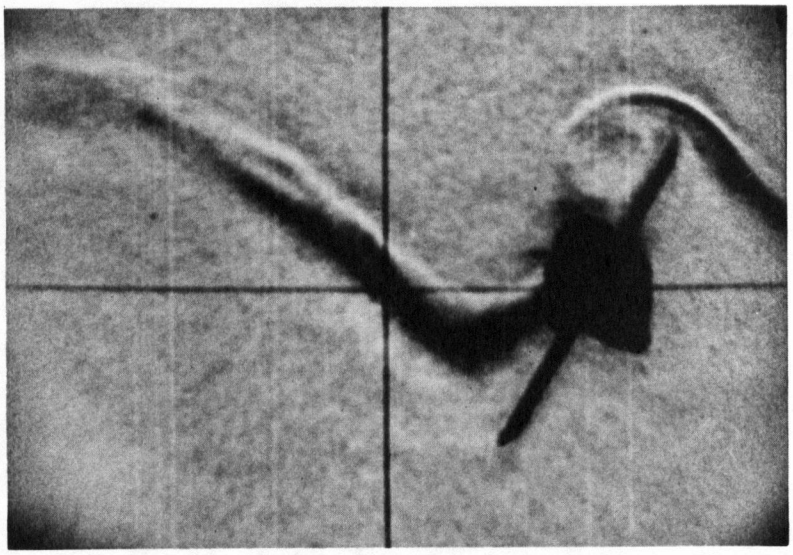

$\alpha = 76°$

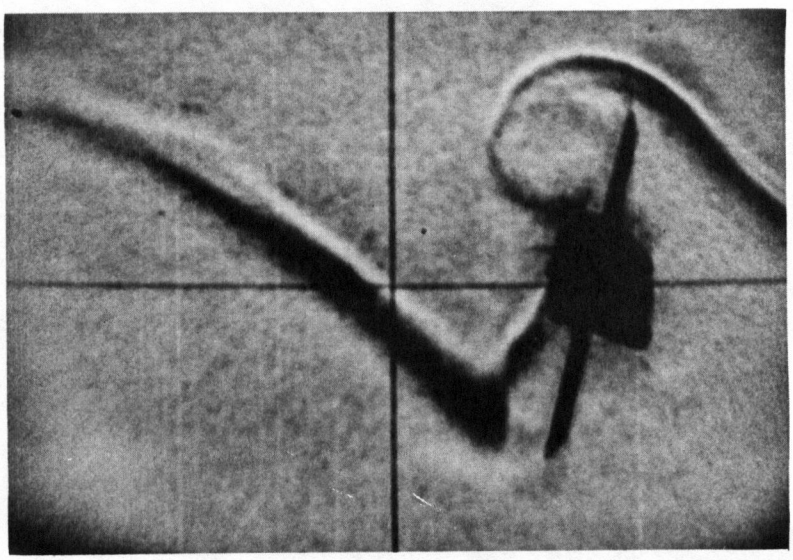

FIG. 13 16mm. MOVIE FILM FRAMES
U = 11.3 ft./sec.

$\alpha = 90°$

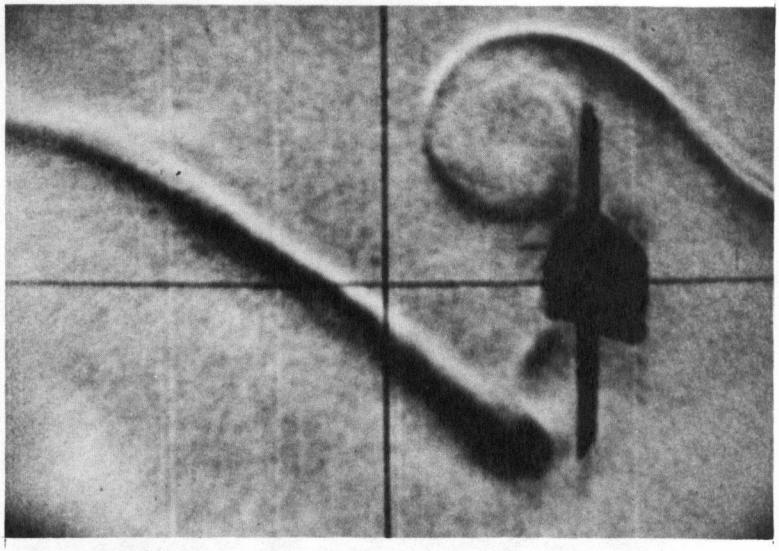

$\alpha = 105°$

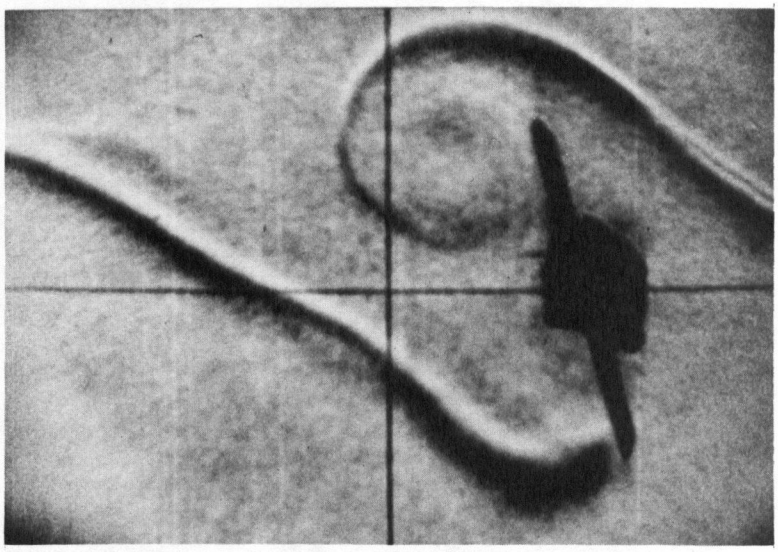

$\alpha = 119°$

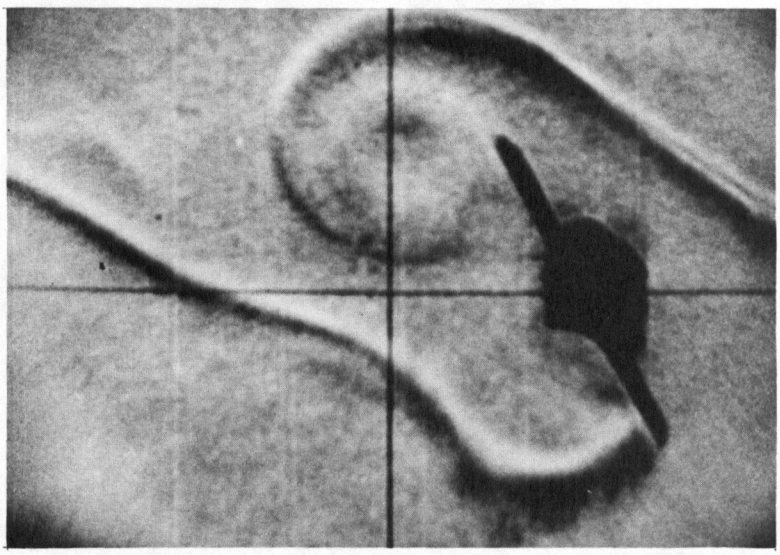

FIG. 14 16mm. MOVIE FILM FRAMES
U = 11.3 ft./sec.

$\alpha = 135°$

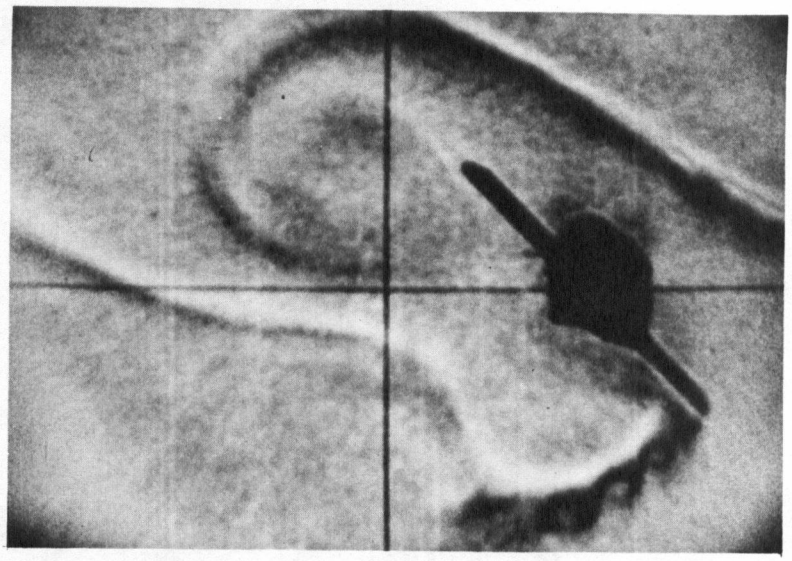

$\alpha = 151°$

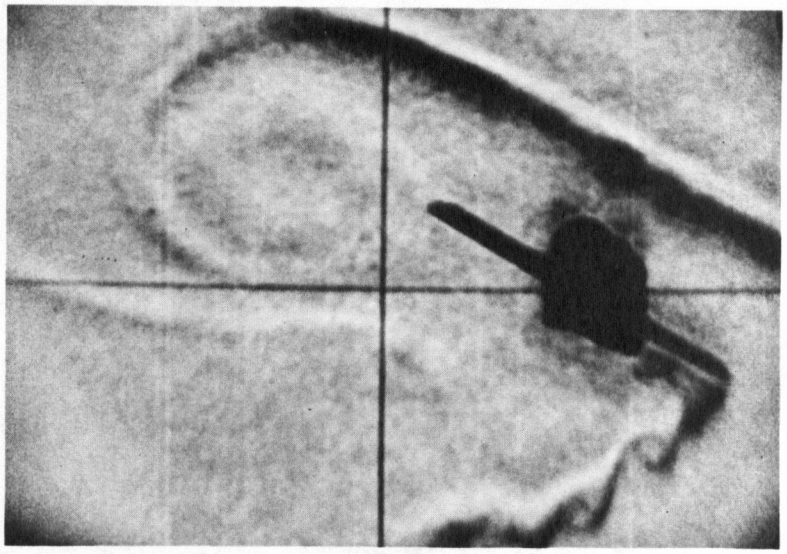

$\alpha = 166°$

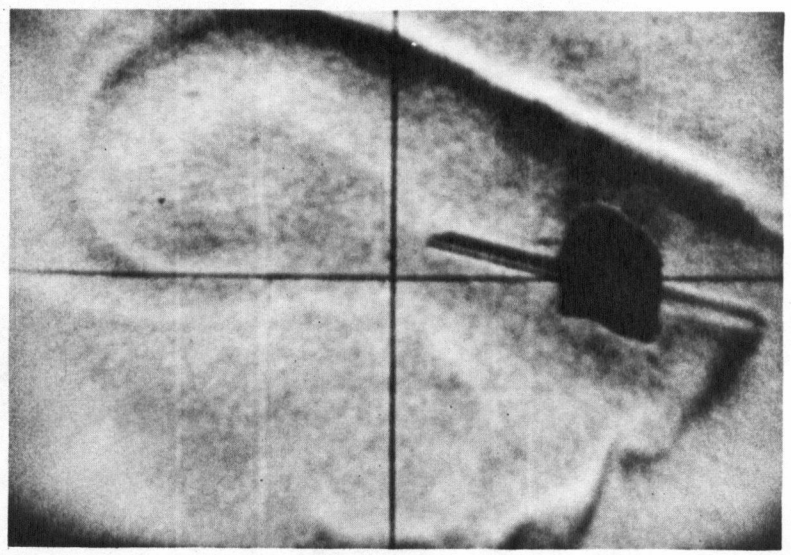

FIG. 15 16mm. MOVIE FILM FRAMES
U = 11.3 ft./sec.

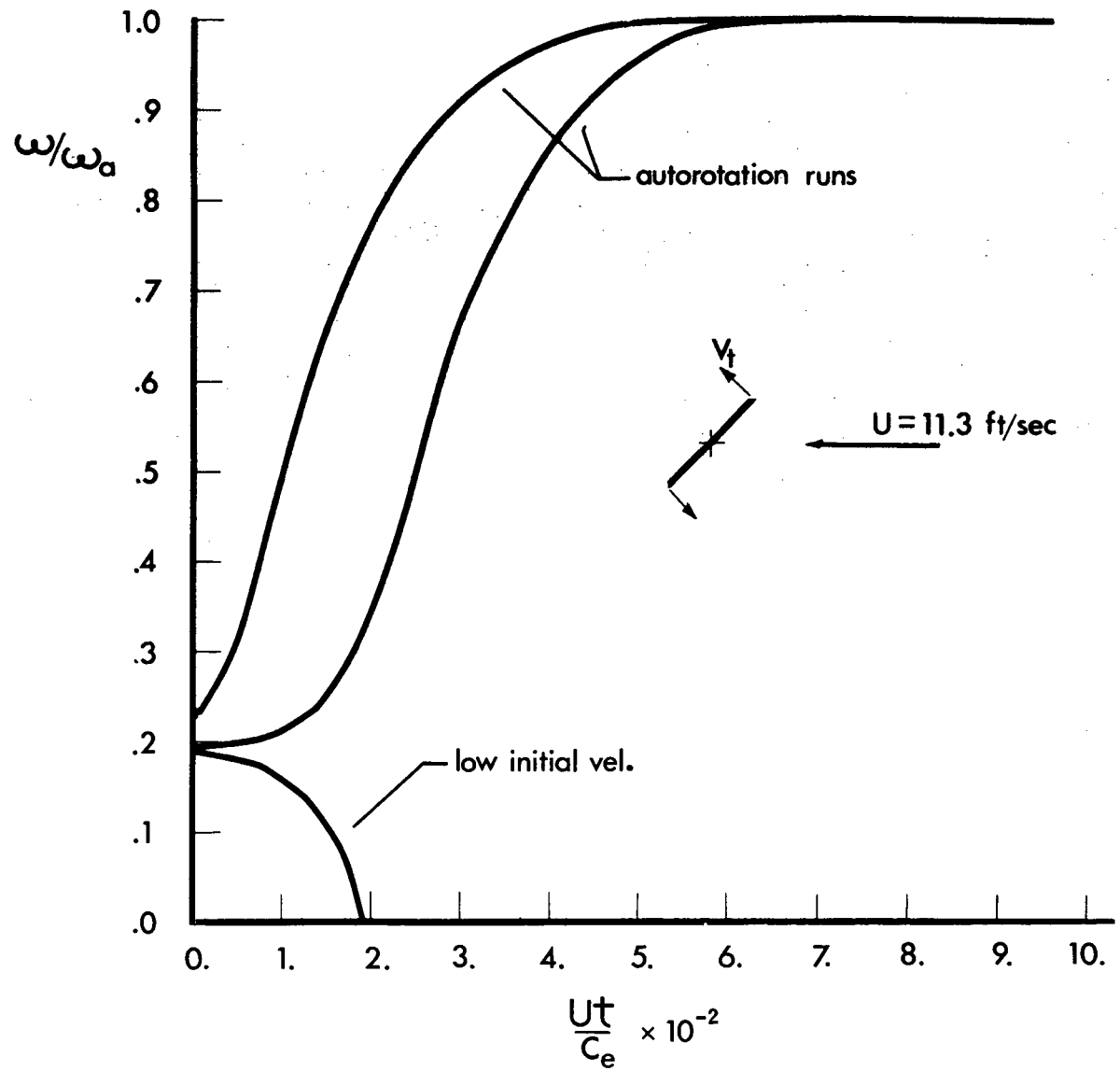

FIG. 16 NON-DIMENSIONALIZED ANGULAR VELOCITY-TIME CURVES FOR ACCELERATION PERIOD U = 11.3 ft./sec.

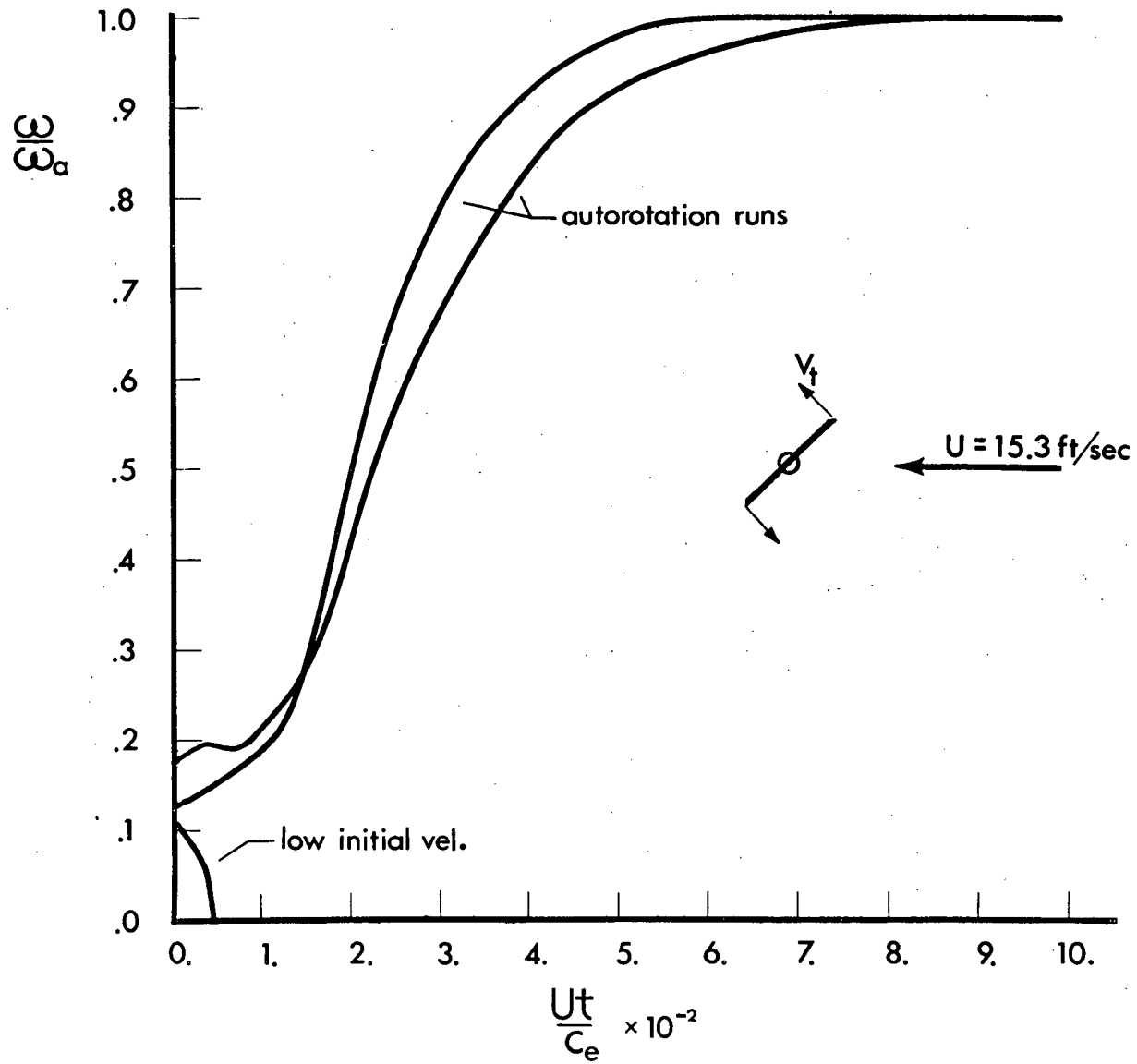

FIG. 17 NON-DIMENSIONALIZED ANGULAR VELOCITY-TIME CURVES FOR ACCELERATION PERIOD U = 15.3 ft./sec.

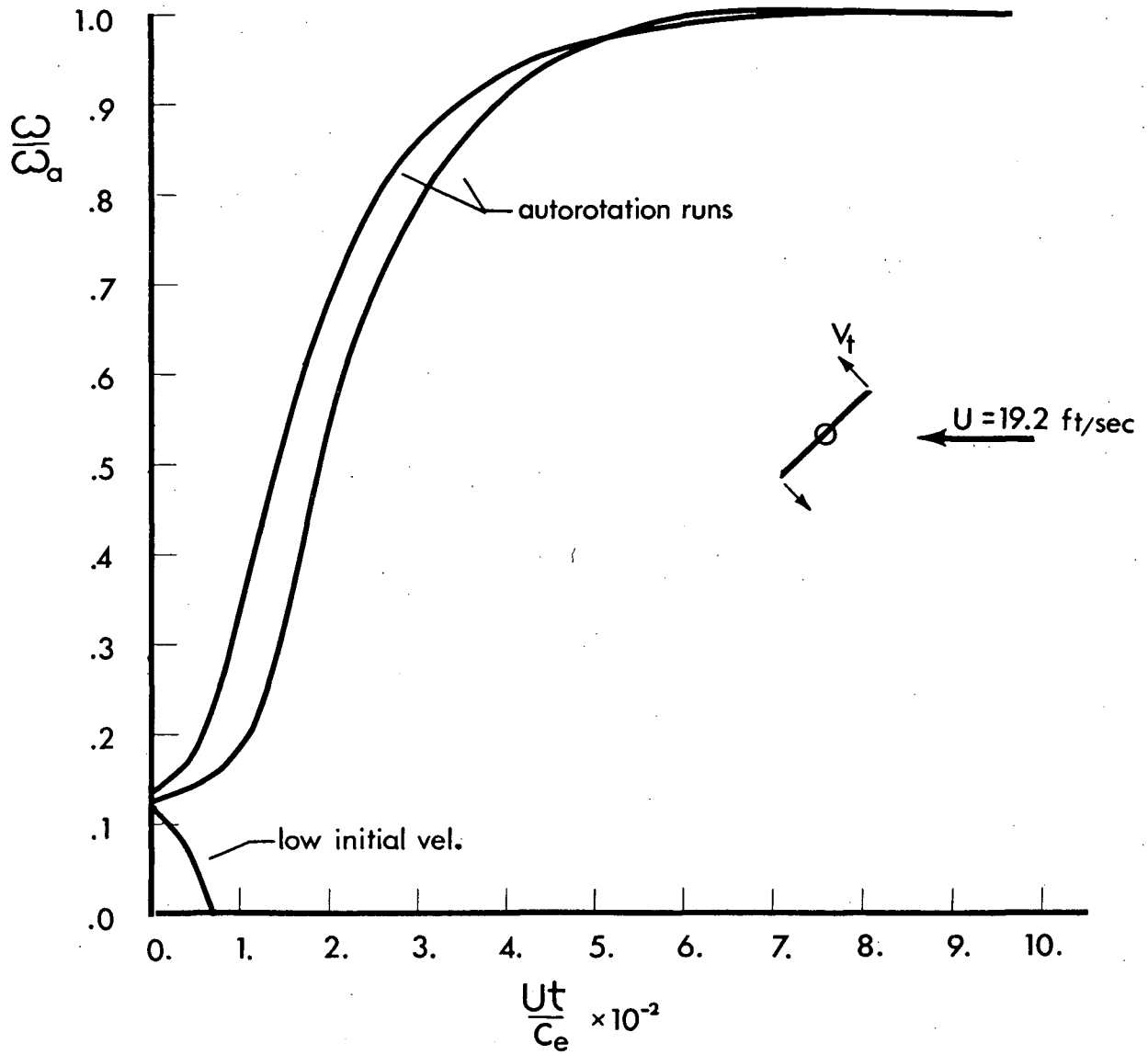

FIG. 18 NON-DIMENSIONALIZED ANGULAR VELOCITY-TIME CURVES FOR ACCELERATION PERIOD U = 19.2 ft./sec.

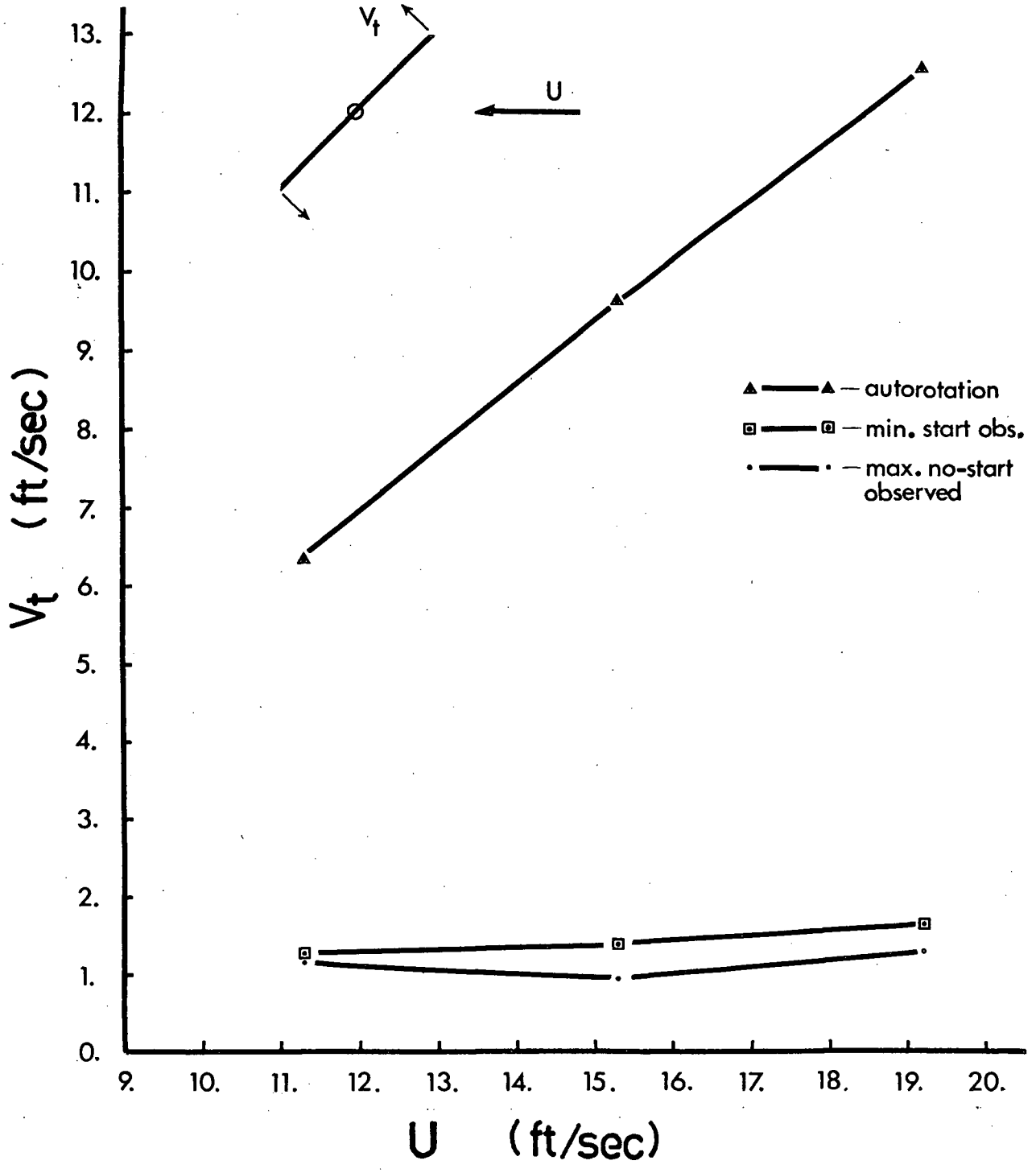

FIG. 19 TIP VELOCITY-FREESTREAM VELOCITY CURVES AT AUTOROTATION AND INITIAL VELOCITY

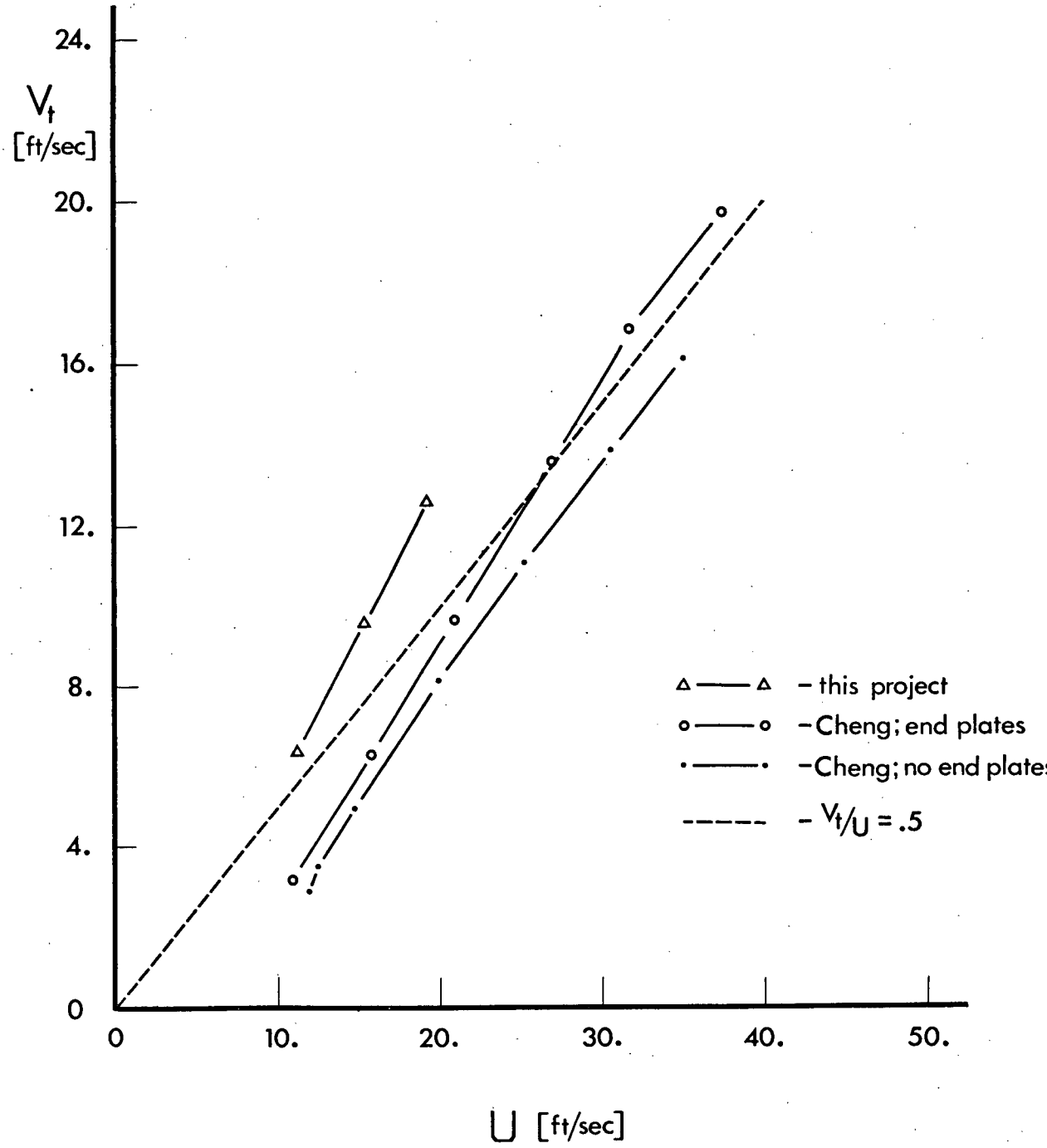

FIG. 20 TIP-FREESTREAM VELOCITY AT AUTOROTATION COMPARED TO CHENG'S RESULTS

IV. THEORETICAL MODEL

4.1 GENERAL OUTLINE

The main purpose for this two-dimensional irrotational incompressible flow model is to predict as accurately as possible the pressure loadings on the plate; that is, to make the model agree as closely as possible with Cheng's measured instantaneous pressure coefficients (uncorrected for tunnel wall effect).

As a starting point, a technique for obtaining the field complex potential from a boundary condition on a rotating translating cylinder (a specific example is an ellipse, or in one limit, a flat plate) is given by Milne-Thomson (6).

Thus, we are able to obtain the complex potential for an attached flow model of a rotating translating flat plate. This gives reasonable results for regions of the actual flow which are attached, but of course when the flow separates (points of separation fixed at the sharp edges) the model prediction is unreasonable.

To improve this, three stationary (with respect to the plate) vortices are superimposed on the attached flow model in the wake region.

To better simulate a wake region for the purpose of calculating pressure coefficients on the plate itself, those terms which represent the effect of the freestream are gradually eliminated on the separated side above the relative zero angle of attack (α_o) and below 180 degrees angle of attack.

Thus, an unsteady modified attached flow (therefore predicting infinite pressure coefficients at the sharp edges) model is constructed for an unsteady separated flow situation.

4.2 COMPLEX POTENTIAL FOR A ROTATING TRANSLATING FLAT PLATE

As stated before, the method for obtaining the complex potential for any rotating translating cyclinder is given by Milne-Thomson (6).

Briefly, one set of co-ordinate axes (Z') is fixed with respect to a translating rotating cylinder which is moving with respect to a fixed set of co-ordinate axes (Z). The situation is considered at an instant when the two sets of axes coincide and the observer is stationary with respect to the Z plane. Referring to figure 21, the cylinder is at the origin rotating with angular velocity ω, translating with velocity U at an angle of attack α.

A boundary relation is obtained from the normal velocity at the surface of the cylinder

$$V_n = -\partial\psi/\partial s$$

since the normal velocity of the fluid at the boundary must match the normal velocity of the boundary.

Integrating the expression for V_n,

$$2i\psi = Ue^{-i\alpha}z - Ue^{i\alpha}\bar{z} - i\omega z\bar{z} + g(n,t)$$

The function of the normal co-ordinate and time is a constant since the relation is valid only on the boundary and is considered at an instant of time when the cylinder axis is coincident with the fixed frame of reference. Therefore, disregarding a constant, the boundary relation is

$$2i\psi = Ue^{-i\alpha}z - Ue^{i\alpha}\bar{z} - i\omega z\bar{z} \qquad 1$$

on γ (fig. 21)

$$\sigma = e^{i\phi} \qquad \bar{\sigma} = 1/\sigma$$

$$2i\psi = F(\sigma) - \bar{F}(\bar{\sigma}) = F(\sigma) - \bar{F}(1/\sigma) \qquad 2$$

Define

$$B(\sigma) = 2i\psi \qquad 3$$

Since $B(\sigma)$ is an analytic function, it can be expanded in a Laurent series.

i.e.

$$B(\sigma) = B_1(\sigma) + B_2(\sigma)$$

where $B_1(\sigma)$ contains all negative powers of σ and $B_2(\sigma)$ contains all other powers. Therefore, $B_1(\sigma)$ is regular outside γ.

By applying Cauchy's integral formula and noting that there are no singularities in the flow field outside γ,

$$F(\zeta) = B_1(\zeta)$$

where ζ is a point outside γ.

Now, for a rotating translating ellipse, as in figure 19, from relations 1 and 3

$$B(\sigma) = Ue^{-i\alpha} W(\sigma + \lambda/\sigma) - Ue^{i\alpha} W(1/\sigma + \lambda\sigma) - i\omega W^2(\sigma + \lambda/\sigma)(1/\sigma + \lambda\sigma)$$

$$\therefore B_1(\sigma) = -U(b\cos\alpha + ia\sin\alpha)\frac{1}{\sigma} - i\omega(a^2 - b^2)\frac{1}{4\sigma^2}$$

$$\therefore F(\zeta) = -U(b\cos\alpha + ia\sin\alpha)\frac{1}{\zeta} - i\omega(a^2 - b^2)\frac{1}{4\zeta^2}$$

For a flat plate $W = 1$ and $\lambda = 1$ or $b = 0$ and $a = 2$.

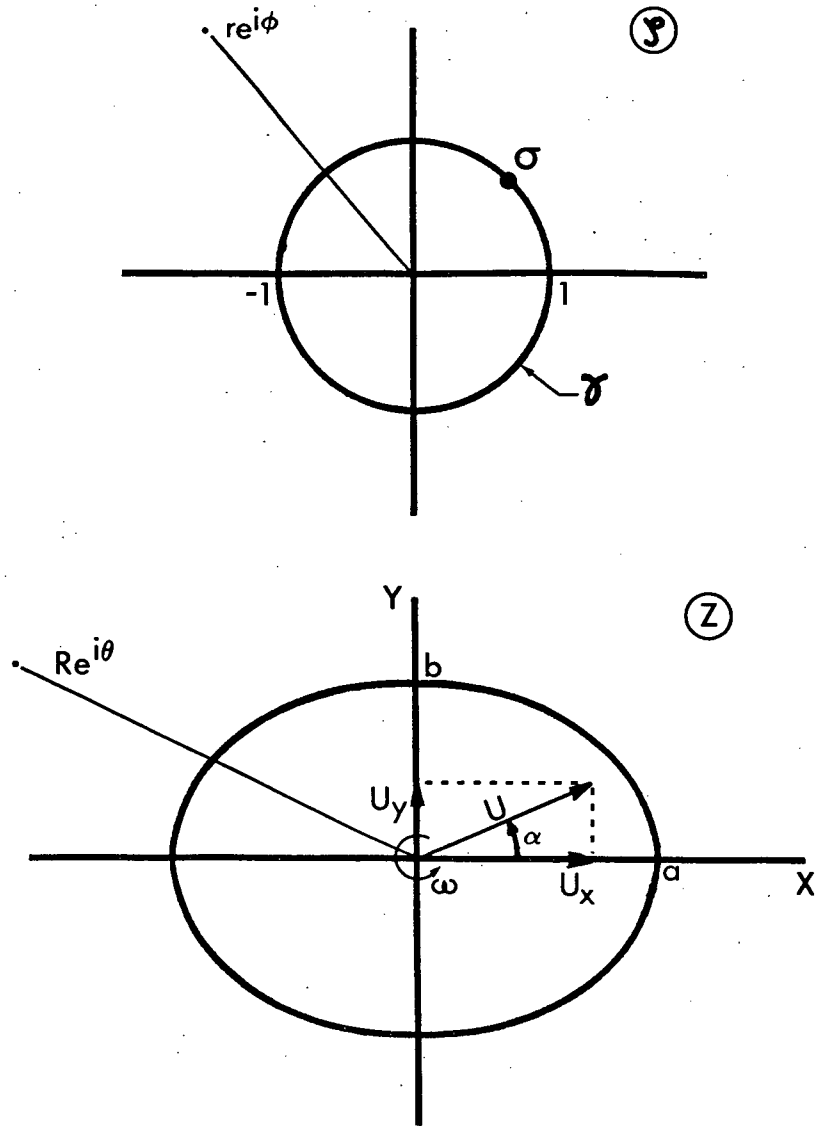

$$Z = W(\zeta + \lambda/\zeta)$$

where; $W = (a+b)/2$

$$\lambda = (a-b)/(a+b)$$

Flat plate: $a=2$ & $b=0$ $\therefore W=1$ & $\lambda=1$

FIG. 21 CONFORMAL TRANSFORMATION FROM UNIT CIRCLE TO ELLIPSE PLANE

4.3 VORTEX SUPERPOSITION

By referring to figure 22 and keeping the Milne-Thomson circle theorem (6) in mind, the complex potential for three fixed vortices in the presence of a unit circle is

$$F(\zeta) = \frac{i\Gamma_1}{2\pi}\left\{\ln(\zeta - s_1 e^{i\delta_1}) - \ln(1/\zeta - s_1 e^{-i\delta_1})\right\} + \frac{i\Gamma_2}{2\pi}\left\{\ln(\zeta - s_2 e^{i\delta_2}) - \ln(1/\zeta - s_2 e^{-i\delta_2})\right\} + \frac{i\Gamma_3}{2\pi}\left\{\ln(\zeta - s_3 e^{i\delta_3}) - \ln(1/\zeta - s_3 e^{-i\delta_3})\right\}$$

Dropping constants

$$F(\zeta) = \frac{i\Gamma_1}{2\pi}\left\{\ln(\zeta - s_1 e^{i\delta_1}) + \ln\zeta - \ln(\zeta - \tfrac{1}{s_1} e^{i\delta_1})\right\} + \frac{i\Gamma_2}{2\pi}\left\{\ln(\zeta - s_2 e^{i\delta_2}) + \ln\zeta - \ln(\zeta - \tfrac{1}{s_2} e^{i\delta_2})\right\} + \frac{i\Gamma_3}{2\pi}\left\{\ln(\zeta - s_3 e^{i\delta_3}) + \ln\zeta - \ln(\zeta - \tfrac{1}{s_3} e^{i\delta_3})\right\}$$

Now this represents, for example in the case of Γ_1, a clockwise vortex at $s_1 e^{i\delta_1}$, an anti-clockwise vortex at $\frac{1}{s_1} e^{i\delta_1}$, and a clockwise vortex at the origin, all of strength Γ_1. Therefore, for a zero net circulation an anti-clockwise circulation of strength Γ_1 is added at the origin. The final complex potential then for three vortices in the presence of a unit circle with zero net circulation is

$$F(\zeta) = \frac{i\Gamma_1}{2\pi}\left\{\ln(\zeta - s_1 e^{i\delta_1}) - \ln(\zeta - \tfrac{1}{s_1} e^{i\delta_1})\right\} + \frac{i\Gamma_2}{2\pi}\left\{\ln(\zeta - s_2 e^{i\delta_2}) - \ln(\zeta - \tfrac{1}{s_2} e^{i\delta_2})\right\} + \frac{i\Gamma_3}{2\pi}\left\{\ln(\zeta - s_3 e^{i\delta_3}) - \ln(\zeta - \tfrac{1}{s_3} e^{i\delta_3})\right\}$$

By conformal transformation to the ellipse plane (Fig. 22), the ellipse becomes a streamline in the presence of external vortices. Since the boundary relation, as derived in section 4.2, was obtained from an integration involving the known normal velocity on a rotating translating ellipse, the vortices may be superimposed, since their contribution to the normal velocity at the boundary is zero.

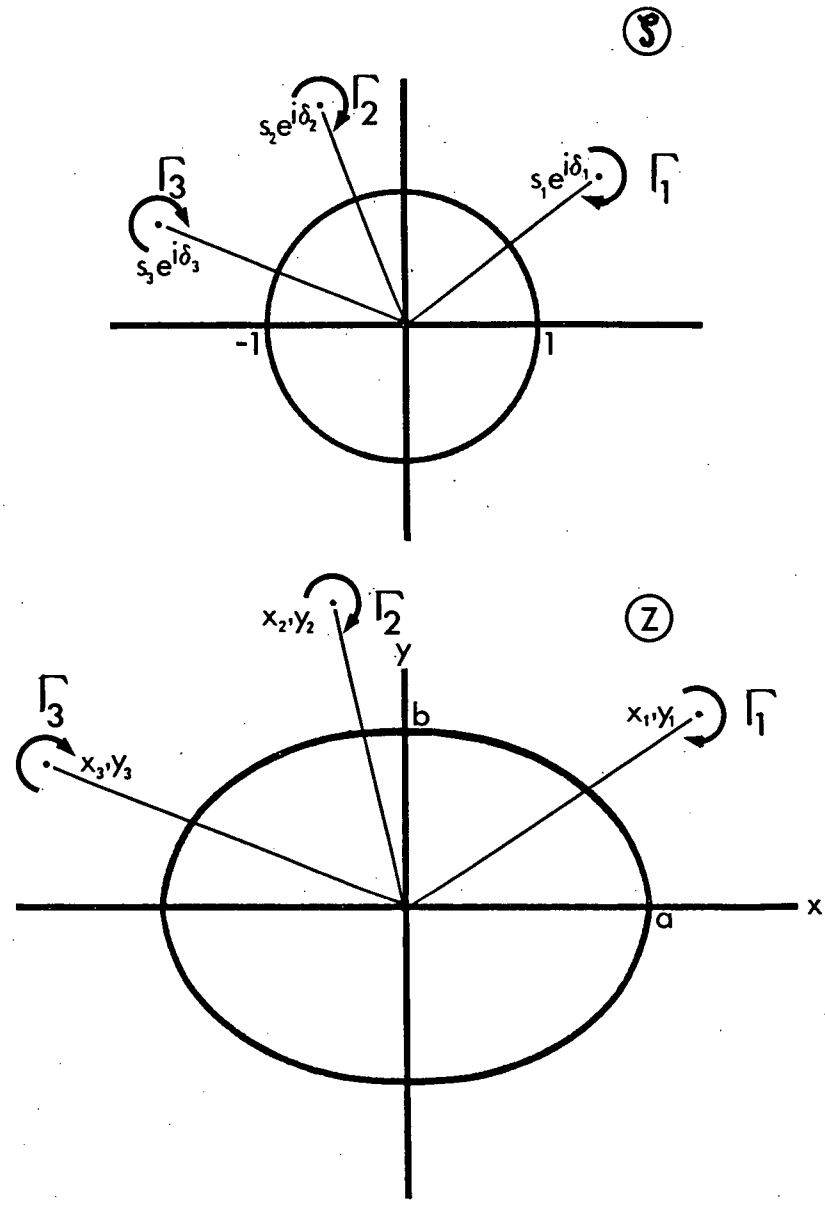

$$Z = W(\zeta + \lambda/\zeta) \qquad \text{where:} \quad W = (a+b)/2$$

$$X_1 = W(S_1 + \lambda/S_1)\cos\delta_1 \qquad \lambda = (a-b)/(a+b)$$

$$Y_1 = W(S_1 - \lambda/S_1)\sin\delta_1$$

FIG. 22 VORTEX CONFORMAL TRANSFORMATION FROM UNIT CIRCLE TO ELLIPSE PLANE

4.4 MODEL PRESSURE COEFFICIENT

The unsteady Bernoulli equation for a translating body at the origin is

$$\partial\Phi/\partial t + p/\rho + |W(z)|^2/2 = K(t) = p_\infty/\rho$$

$$C_p = \frac{p - p_\infty}{\frac{\rho}{2}U^2}$$

$$= -\frac{2}{U^2}\left(\frac{\partial\Phi}{\partial t}\right) - \frac{|W(z)|^2}{U^2}$$

As stated before, for calculating the pressure coefficient on the plate and to better simulate a separated region (that is r = 1 and $0° \leq \phi \leq 180°$), those terms representing the effect of the freestream are gradually eliminated on the separated side above 30 degrees and below 180 degrees angle of attack. Those terms affected are underlined by a dashed line in the following work and for the elimination factor ϵ as a function of angle of attack, refer to figure 24.

The lower limit of 30 degrees is the zero relative angle of attack for a tip velocity to freestream velocity of 0.5. This approximation is shown in figure 20.

At 180 degrees angle of attack, the pressure distribution as predicted by the model must be the same as at zero degrees angle of attack. Freestream effects start to become important again on the separated side below 60 degrees and above 150 degrees angle of attack and $\epsilon = 1$ at 180 degrees to make the pressure loading equivalent to that at zero degrees angle of attack.

Thus, between the above limits the only effect of the freestream on the separated side is to control the magnitude of the generated vorticity.

a) complex velocity magnitude $|W(z)|$

$$|W(z)|^2 = V_x^2 + V_y^2$$

$$W(z) = V_x - iV_y$$

$$= \frac{dF(\zeta)}{d\zeta} \Big/ \frac{dz}{d\zeta}$$

$$z = W(\zeta + \lambda/\zeta)$$

$$\frac{dz}{d\zeta} = W(1 - \lambda/\zeta^2)$$

Now

$$\frac{dF(\zeta)}{d\zeta} = U(b\cos\alpha + ia\sin\alpha)\frac{1}{\zeta^2} + \frac{i\omega}{2}\frac{(a^2-b^2)}{\zeta^3}$$

$$+ \frac{i\Gamma_1}{2\pi}\left\{\frac{1}{\zeta - s_1 e^{i\delta_1}} - \frac{1}{\zeta - \frac{1}{s_1}e^{i\delta_1}}\right\} + \frac{i\Gamma_2}{2\pi}\left\{\frac{1}{\zeta - s_2 e^{i\delta_2}} - \frac{1}{\zeta - \frac{1}{s_2}e^{i\delta_2}}\right\}$$

$$+ \frac{i\Gamma_3}{2\pi}\left\{\frac{1}{\zeta - s_3 e^{i\delta_3}} - \frac{1}{\zeta - \frac{1}{s_3}e^{i\delta_3}}\right\}$$

Separating real and imaginary parts and introducing ϵ gives

$$V_x = \frac{1}{D}\Big[\epsilon\frac{U}{r^2}(b\cos\alpha\cos 2\phi + a\sin\alpha\sin 2\phi) + \frac{\omega(a^2-b^2)}{2r^3}\sin 3\phi$$

$$- \frac{\Gamma_1}{2\pi}\mathrm{Im}\{I\} - \frac{\Gamma_2}{2\pi}\mathrm{Im}\{II\} - \frac{\Gamma_3}{2\pi}\mathrm{Im}\{III\} - \epsilon\frac{U\lambda b\cos\alpha}{r^4}$$

$$- \frac{\omega(a-b)^2}{2r^5}\sin\phi + \frac{\Gamma_1\lambda}{2\pi r^2}\left(\mathrm{Re}\{I\}\sin 2\phi + \mathrm{Im}\{I\}\cos 2\phi\right)$$

$$+ \frac{\Gamma_2\lambda}{2\pi r^2}\left(\mathrm{Re}\{II\}\sin 2\phi + \mathrm{Im}\{II\}\cos 2\phi\right)$$

$$+ \frac{\Gamma_3\lambda}{2\pi r^2}\left(\mathrm{Re}\{III\}\sin 2\phi + \mathrm{Im}\{III\}\cos 2\phi\right)\Big]$$

$$V_y = -\frac{1}{D}\Big[\epsilon\frac{U}{r^2}(-b\cos\alpha\sin 2\phi + a\sin\alpha\cos 2\phi) + \frac{\omega(a^2-b^2)}{2r^3}\cos 3\phi$$

$$+ \frac{\Gamma_1}{2\pi}Re\{I\} + \frac{\Gamma_2}{2\pi}Re\{II\} + \frac{\Gamma_3}{2\pi}Re\{III\} - \epsilon\frac{U\lambda a\sin\alpha}{r^4}$$

$$- \frac{\omega(a-b)^2}{2r^5}\cos\phi + \frac{\Gamma_1\lambda}{2\pi r^2}\left(-Re\{I\}\cos 2\phi + Im\{I\}\sin 2\phi\right)$$

$$+ \frac{\Gamma_2\lambda}{2\pi r^2}\left(-Re\{II\}\cos 2\phi + Im\{II\}\sin 2\phi\right)$$

$$+ \frac{\Gamma_3\lambda}{2\pi r^2}\left(-Re\{III\}\cos 2\phi + Im\{III\}\sin 2\phi\right)$$

where

$$D = W\left(1 - \frac{2\lambda}{r^2}\cos 2\phi + \frac{\lambda^2}{r^4}\right)$$

$$Re\{I\} = \frac{r\cos\phi - s_1\cos\delta_1}{r^2 + s_1^2 - 2s_1 r\cos(\phi-\delta_1)} - \frac{r\cos\phi - \frac{1}{s_1}\cos\delta_1}{r^2 + \frac{1}{s_1^2} - \frac{2r}{s_1}\cos(\phi-\delta_1)}$$

$$Im\{I\} = -\frac{r\sin\phi - s_1\sin\delta_1}{r^2 + s_1^2 - 2s_1 r\cos(\phi-\delta_1)} + \frac{r\sin\phi - \frac{1}{s_1}\sin\delta_1}{r^2 + \frac{1}{s_1^2} - \frac{2r}{s_1}\cos(\phi-\delta_1)}$$

$$Re\{II\} = Re\{I\}\Big|_{\substack{\delta_1\to\delta_2 \\ s_1\to s_2}} \qquad Im\{II\} = Im\{I\}\Big|_{\substack{\delta_1\to\delta_2 \\ s_1\to s_2}}$$

$$Re\{III\} = Re\{I\}\Big|_{\substack{\delta_1\to\delta_3 \\ s_1\to s_3}} \qquad Im\{III\} = Im\{I\}\Big|_{\substack{\delta_1\to\delta_3 \\ s_1\to s_3}}$$

b) $\partial\Phi/\partial t$

By definition (refer to figure 23)

$$\partial\Phi/\partial t \equiv \partial/\partial t \, \mathrm{Real}\{F(\zeta)\}$$

$$= \lim_{\Delta t \to 0} \left[\frac{\Phi(t+\Delta t, P) - \Phi(t, P)}{\Delta t} \right]$$

To obtain the velocity potential at $t+\Delta t$ and at point P, consider the rotating translating ellipse at the origin, as shown in figure 23. The point P moves to point P' with respect to the ellipse in time Δt.

$$\partial\Phi/\partial t = \lim_{\Delta t \to 0} \left[\frac{\Phi(P') - \Phi(P)}{\Delta t} \right]$$

$$= \lim_{\Delta t \to 0} \left[\frac{\Phi(x'; y'; \alpha'; \Gamma_1'; \Gamma_2'; \Gamma_3') - \Phi(x, y; \alpha; \Gamma_1; \Gamma_2; \Gamma_3)}{\Delta t} \right]$$

$$= \frac{\partial\Phi}{\partial x}\frac{\Delta x}{\Delta t} + \frac{\partial\Phi}{\partial y}\frac{\Delta y}{\Delta t} + \frac{\partial\Phi}{\partial\alpha}\frac{\partial\alpha}{\partial t} + \frac{\partial\Phi}{\partial\Gamma_1}\frac{\partial\Gamma_1}{\partial t} + \frac{\partial\Phi}{\partial\Gamma_2}\frac{\partial\Gamma_2}{\partial t} + \frac{\partial\Phi}{\partial\Gamma_3}\frac{\partial\Gamma_3}{\partial t}$$

$$= V_x \frac{\Delta x}{\Delta t} + V_y \frac{\Delta y}{\Delta t} + \frac{\partial\Phi}{\partial\alpha}\frac{\partial\alpha}{\partial t} + \frac{\partial\Phi}{\partial\Gamma_1}\frac{\partial\Gamma_1}{\partial t} + \frac{\partial\Phi}{\partial\Gamma_2}\frac{\partial\Gamma_2}{\partial t} + \frac{\partial\Phi}{\partial\Gamma_3}\frac{\partial\Gamma_3}{\partial t}$$

now

$$P' = R\cos(\theta - \omega\Delta t) - U\Delta t\cos\alpha + i\{R\sin(\theta - \omega\Delta t) - U\Delta t\sin\alpha\}$$

$$= R\cos\theta + (R\omega\sin\theta - U\cos\alpha)\Delta t + i\{R\sin\theta - (R\omega\cos\theta + U\sin\alpha)\Delta t\}$$

$$\therefore \frac{\Delta x}{\Delta t} = R\omega\sin\theta - U\cos\alpha$$

$$= \omega y - \underline{\epsilon U\cos\alpha}$$

$$\frac{\Delta y}{\Delta t} = -(R\omega\cos\theta + U\sin\alpha)$$

$$= -\omega x - \underline{\epsilon U\sin\alpha}$$

now

$$\alpha = -\omega t$$

$$\therefore \frac{\partial \alpha}{\partial t} = -\omega$$

$$\Phi(S) = Real\{F(S)\}$$

$$= -\frac{U}{r}(b\cos\alpha\cos\phi + a\sin\alpha\sin\phi) - \frac{\omega(a^2-b^2)}{4r^2}\sin 2\phi$$
$$+ \frac{\Gamma_1}{2\pi}\left\{\tan^{-1}\left(\frac{r\sin\phi - \frac{1}{S_1}\sin\delta_1}{r\cos\phi - \frac{1}{S_1}\cos\delta_1}\right) - \tan^{-1}\left(\frac{r\sin\phi - S_1\sin\delta_1}{r\cos\phi - S_1\cos\delta_1}\right)\right\}$$
$$+ \frac{\Gamma_2}{2\pi}\left\{\tan^{-1}\left(\frac{r\sin\phi - \frac{1}{S_2}\sin\delta_2}{r\cos\phi - \frac{1}{S_2}\cos\delta_2}\right) - \tan^{-1}\left(\frac{r\sin\phi - S_2\sin\delta_2}{r\cos\phi - S_2\cos\delta_2}\right)\right\}$$
$$+ \frac{\Gamma_3}{2\pi}\left\{\tan^{-1}\left(\frac{r\sin\phi - \frac{1}{S_3}\sin\delta_3}{r\cos\phi - \frac{1}{S_3}\cos\delta_3}\right) - \tan^{-1}\left(\frac{r\sin\phi - S_3\sin\delta_3}{r\cos\phi - S_3\cos\delta_3}\right)\right\}$$

$$\frac{\partial \Phi}{\partial \Gamma_1} = \frac{1}{2\pi}\left\{\tan^{-1}\left(\frac{r\sin\phi - \frac{1}{S_1}\sin\delta_1}{r\cos\phi - \frac{1}{S_1}\cos\delta_1}\right) - \tan^{-1}\left(\frac{r\sin\phi - S_1\sin\delta_1}{r\cos\phi - S_1\cos\delta_1}\right)\right\}$$

$$\frac{\partial \Phi}{\partial \alpha} = -\epsilon\frac{U}{r}(-b\sin\alpha\cos\phi + a\cos\alpha\sin\phi)$$

4.5 VORTEX STRENGTH AND POSITION ASSUMPTIONS

Three vortices are superimposed in the wake region to represent the effect of separation.

Since the model vortices are fixed with respect to the plate and have only one direction of rotation, the strengths as a function of angle of attack must be zero and have a zero slope at 180 degrees and zero degrees angle of attack to give a continuous cycle.

The strength as a function of angle of attack must be continuous.

The 'dominant' vortex (#1) begins to form as the upstream tip passes through the relative zero angle of attack (30 degrees for a tip velocity to freestream velocity ratio of 0.5). The flow separates at this point and then reattaches to form a separation bubble. As the angle of attack increases, the bubble becomes a vortex, and at approximately 90 degrees the fully developed vortex begins to shed. In Cheng's pressure measurements, the maximum suction for the 'dominant' vortex occurred at tap #12 ($x = 1.436$) at an angle of attack of 75 degrees. Assumptions made for the 'dominant' vortex are that the x co-ordinate equals 1.436 and that the strength is zero up to the relative zero angle of attack and then negative (clockwise positive). Since the vortex is fixed, the magnitude of Γ_1 must increase up to 90 degrees to simulate growth of the vortex, and then decrease as the vortex is shed. The final form of Γ_1 vs α is given in figure 24 and was determined by trial and error computer runs, in an attempt to approximate Cheng's measured pressure loadings.

Visual information on the 'small' vortex (#3) formed on the other tip is fairly limited, which suggests that the strength is less than the 'dominant' vortex. This is supported by Cheng's measurements, in that the maximum suction peak at the 'dominant' vortex is approximately 2.5 times that under the 'small' vortex. The maximum suction for the 'small' vortex

occurs at tap #2 (x = -1.436) and, therefore, the x co-ordinate of the 'small' vortex is fixed at this value. The pressure distribution, as predicted by the attached flow model, is degraded by a circulation generated in the 'small' vortex below the relative zero angle of attack. Therefore, the strength of the 'small' vortex (Fig. 24) is zero up to 30 degrees and returns to zero again at 180 degrees to comply with the restriction of continuity, as mentioned earlier.

Another vortex (#2) is superimposed to represent the effect of the downstream wake; i.e. principally the 'dominant' vortex which formed one-half cycle before. Thus, the maximum magnitude of the 'old' vortex must be assumed to be less than or equal to the maximum magnitude of the 'dominant' vortex. This 'old' vortex appears to move (to an observer on the plate) from a position relatively close to the tip forming the 'small' vortex to a position somewhat more downstream and near 90 degrees relative to the plate, while the angle of attack progresses from zero to 90 degrees. It then moves downstream and its influence to the flow near the plate drops.

It was found that the pressure distribution on the vortex side of the plate was just as dependent on the slope of the Γ vs α curves as the magnitude. Thus, if the slope of one of the circulation per unit span curves is high over a range of angles of attack compared to other angles, a sharp change in the predicted pressure distribution on the vortex side can be expected over that range.

The final form of the circulation per unit span as a function of angle of attack and the y co-ordinate of each vortex (Fig. 24) was then determined by trial and error computer runs, attempting to duplicate Cheng's pressure coefficients.

The assumed functions are:

$\underline{\epsilon}$

$r=1 \qquad 0 \le \phi \le 180°$

$0 \le \alpha < 30° \quad \epsilon = 1$
$30° \le \alpha < 60 \quad \epsilon = \sin^2\{3(\alpha-60)\}$
$60 \le \alpha < 150 \quad \epsilon = 0$
$150 \le \alpha < 180 \quad \epsilon = \sin^2\{3(\alpha-150)\}$

$\underline{\Gamma_1}$

$0 \le \alpha \le 30 \quad \Gamma_1 = 0$
$30 \le \alpha \le 180° \quad \Gamma_1 = -4U\sin^2\{\frac{6}{5}(\alpha-30)\}$

$x = 1.436 \qquad y = 1.0$

$\underline{\Gamma_2}$ $\qquad 0 \le \alpha \le 180° \quad \Gamma_2 = -\frac{1}{2}U\sin^2\alpha$

$x = 0. \qquad y = 4.0$

$\underline{\Gamma_3}$

$0 \le \alpha < 30 \quad \Gamma_3 = 0$
$30 \le \alpha \le 180° \quad \Gamma_3 = U\sin^2\{\frac{6}{5}(\alpha-30)\}$

$x = -1.436 \qquad y = 1.0$

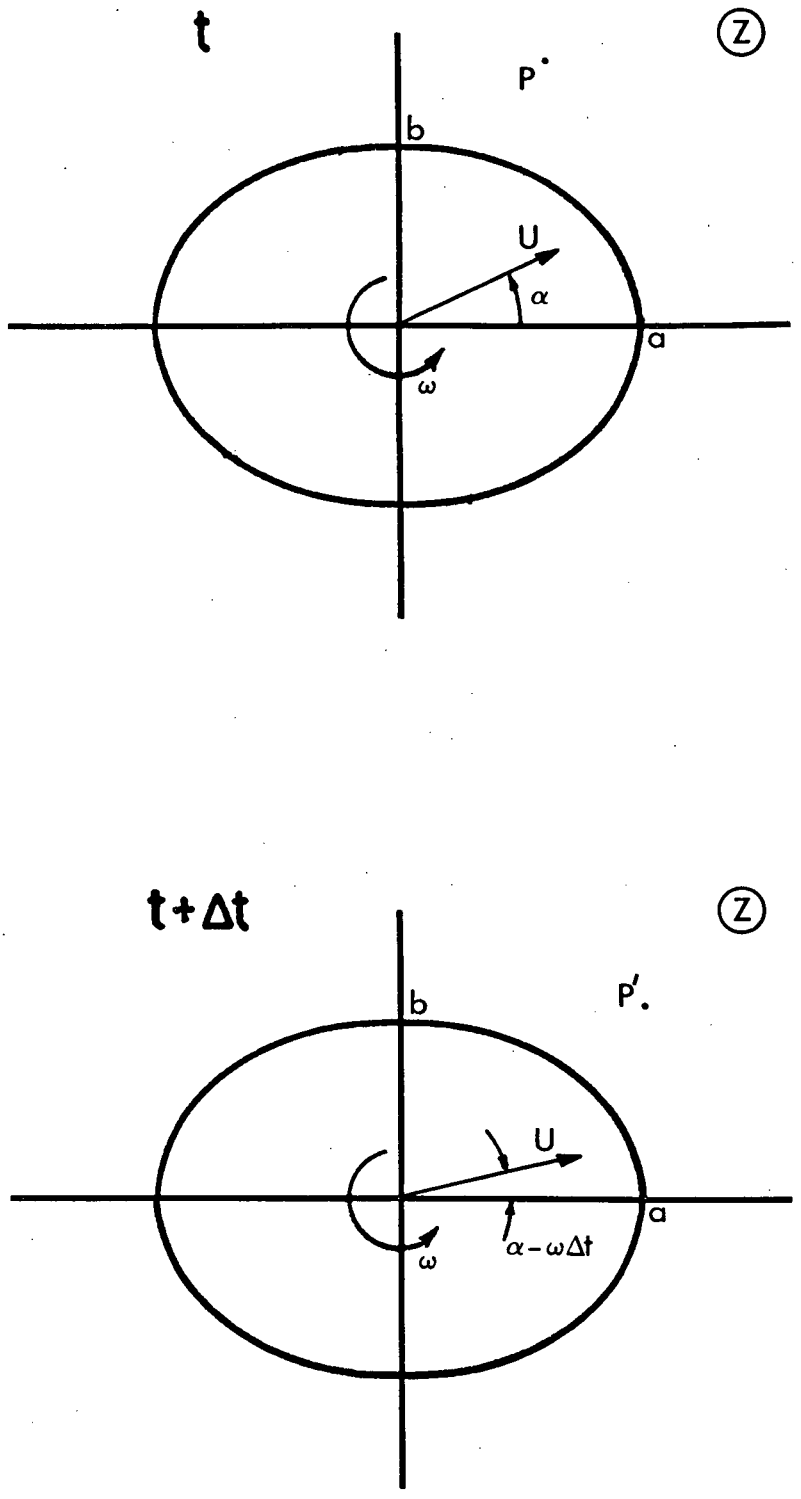

FIG. 23 CYLINDER AT ORIGIN AT TIME t AND $t+\Delta t$

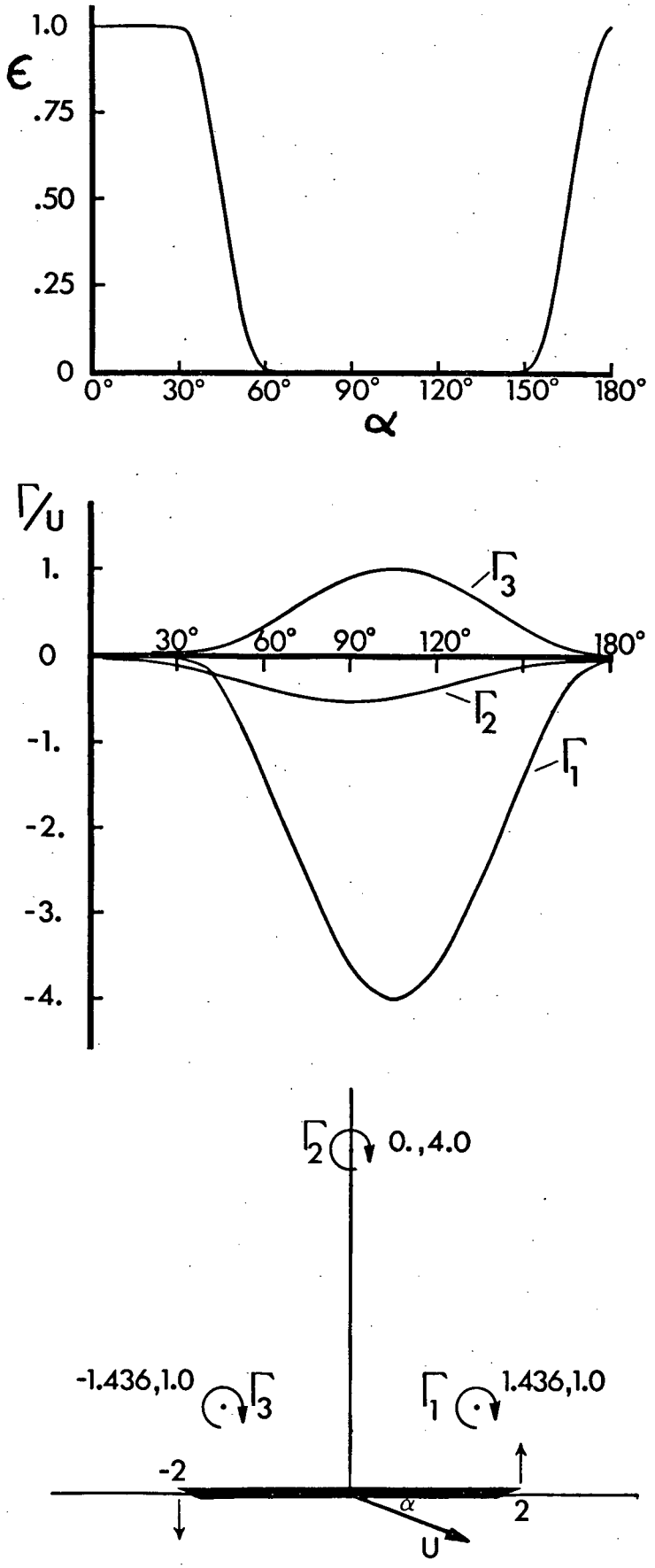

FIG. 24 ELIMINATION FACTOR & CIRCULATION VS ANGLE OF ATTACK AND VORTEX POSITION

V. MODEL RESULTS

The model will be compared to Cheng's (1) pressure loadings and the torque-lift-drag curves derived from these measurements. Cheng obtained these latter curves by assuming that the pressure measured at a tap acted over a finite area around that tap. Thus, the lift, drag and torque acting on the plate could be found as a function of angle of attack. The model was treated in the same manner; that is, the pressure prediction of the model at Cheng's tap positions was used over a finite area to determine the integrated curves shown in figures 31-33.

Pressure coefficients versus position on the plate determined from the model and compared to Cheng's measurements are shown in figures 25-30 for 30 degree intervals in angle of attack from zero to 180 degrees.

Since the model is attached flow, infinite pressure coefficients are given at the edges. At zero degrees, the model predicts a symmetric pressure loading about the axis of rotation. The magnitude of the pressure and general trend is represented quite well, but the smaller variations are not given. Above zero degrees, the symmetry of the model prediction disappears. In figure 26 (α = 30 degrees), the loading trend and magnitude is predicted quite well except as the position approaches zero. Here, a positive pressure is given for experimentally determined suction on the vortex side and a suction prediction for positive pressure on the attached side. As the angle of attack increases further, the trend of the model prediction is accurate but the magnitude of the pressures is not represented, as can be seen in figure 27 (α = 60 degrees). At 60 degrees, a flow detail which is not given by the model is the maximum in the suction pressure near the 'dominant' vortex. The term $\frac{\partial \phi}{\partial \eta}\frac{\partial \Gamma}{\partial t}$, which represents the time rate of change of the 'dominant' vortex strength, does give this but the effect is

completely masked by the term $|w(z)|$ approaching infinity at the edge. At 90 and 120 degree angles of attack, the model again gives the trend of the pressure coefficient but not the magnitude. As the angle increases further, the magnitude prediction again becomes more accurate, as can be seen in figure 30. At 180 degrees, of course, the pressure loading is equal to that at zero degrees.

In figure 31, the drag coefficient curve for the model is compared to Cheng's experimental curve. In both cases, the maximum drag occurs near 90 degrees, but reflecting the model's failure to reach the pressure magnitudes at high angles of incidence the magnitude is not predicted. This is true also of the lift coefficient (Fig. 32). Here, however, the maximum lift is predicted at zero degrees, whereas in fact it occurs near 45 degrees. The torque coefficient (Fig. 33) is quite well represented except for a spike near 30 degrees. This occurs since, as mentioned earlier, the model gives the wrong sign for the pressure coefficient at one end of the plate on both sides. This produces a positive torque contribution rather than negative. The torque at zero degrees is zero, since the model pressure distribution is symmetric about the axis of rotation at $\alpha = 0$.

It must be emphasized that this solution is a compromise based on assumptions of vortex position and strength and the elimination factor ϵ. Thus, although considerable computing time was spent searching for the best assumptions to bring the model into the best possible agreement with the actual flow situation, a better set of assumptions may exist. An example will probably illustrate the compromise involved quite well. In early attempts at assumptions, the strength Γ_2 was equal to Γ_1 up to 90 degrees angle of attack, and then decreased sharply but continuously to 120 degrees. The computer output was being examined at 30 degree intervals from zero to 180 degrees. With this assumption, the suction magnitudes were reached at

60 and 90 degrees and were good at 120 degrees. However, when computer output for the pressure coefficient was produced at 10 degree intervals, the prediction at 100 and 110 degrees showed very high positive pressures rather than suction. This was due to the relatively high value of $\partial\Gamma_3/\partial t$ at these angles.

To improve upon the model, the first step might be to let the vortex position be a function of time, as shown by the flow visualization. Also, the time dependent vortex circulation might be solved for analytically or by iteration to force separation at the edges.

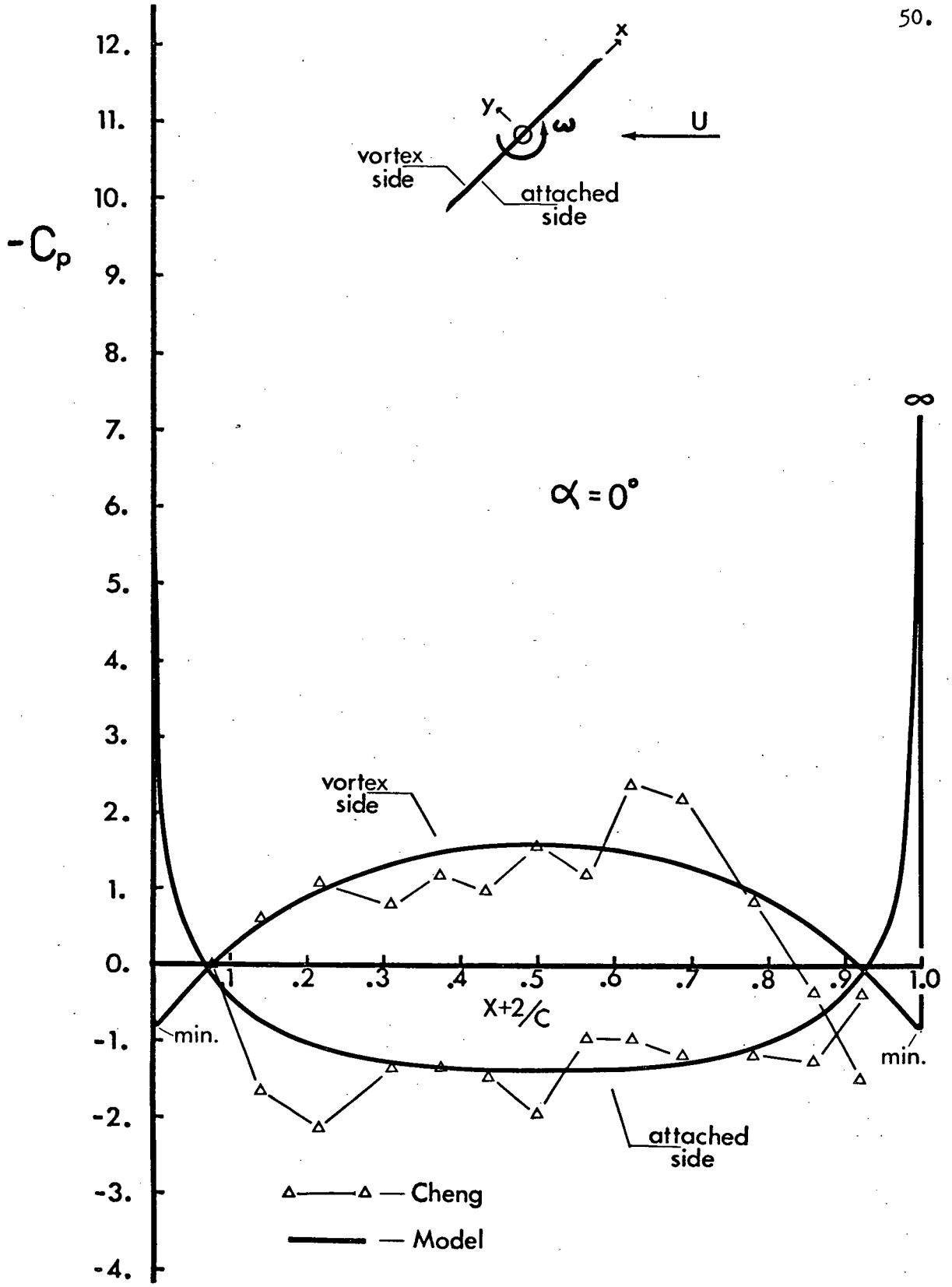

FIG. 25 PRESSURE COEFFICIENT - PLATE POSITION
ANGLE OF ATTACK = 0 DEGREES

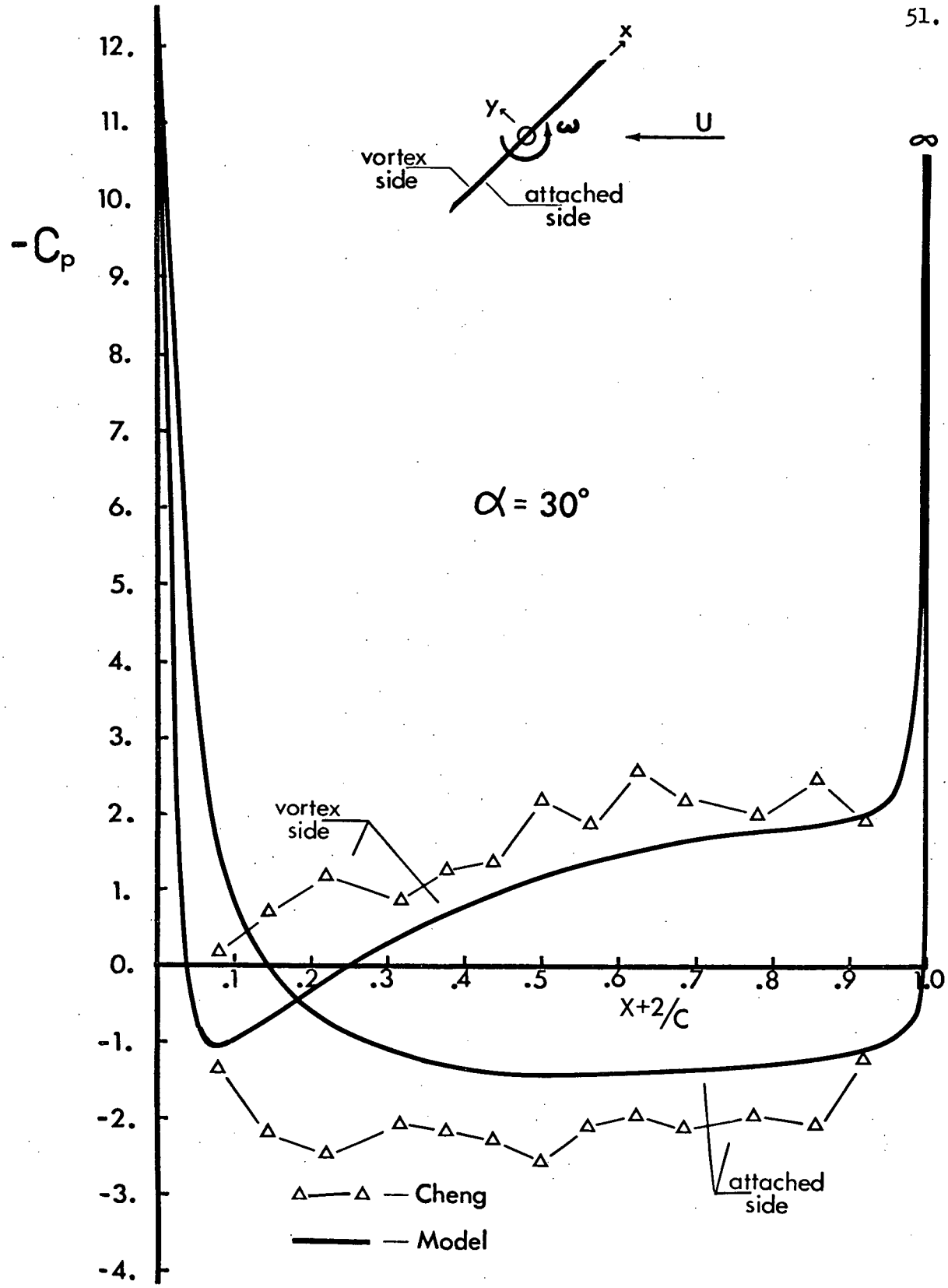

FIG. 26 PRESSURE COEFFICIENT - PLATE POSITION
ANGLE OF ATTACK = 30 DEGREES

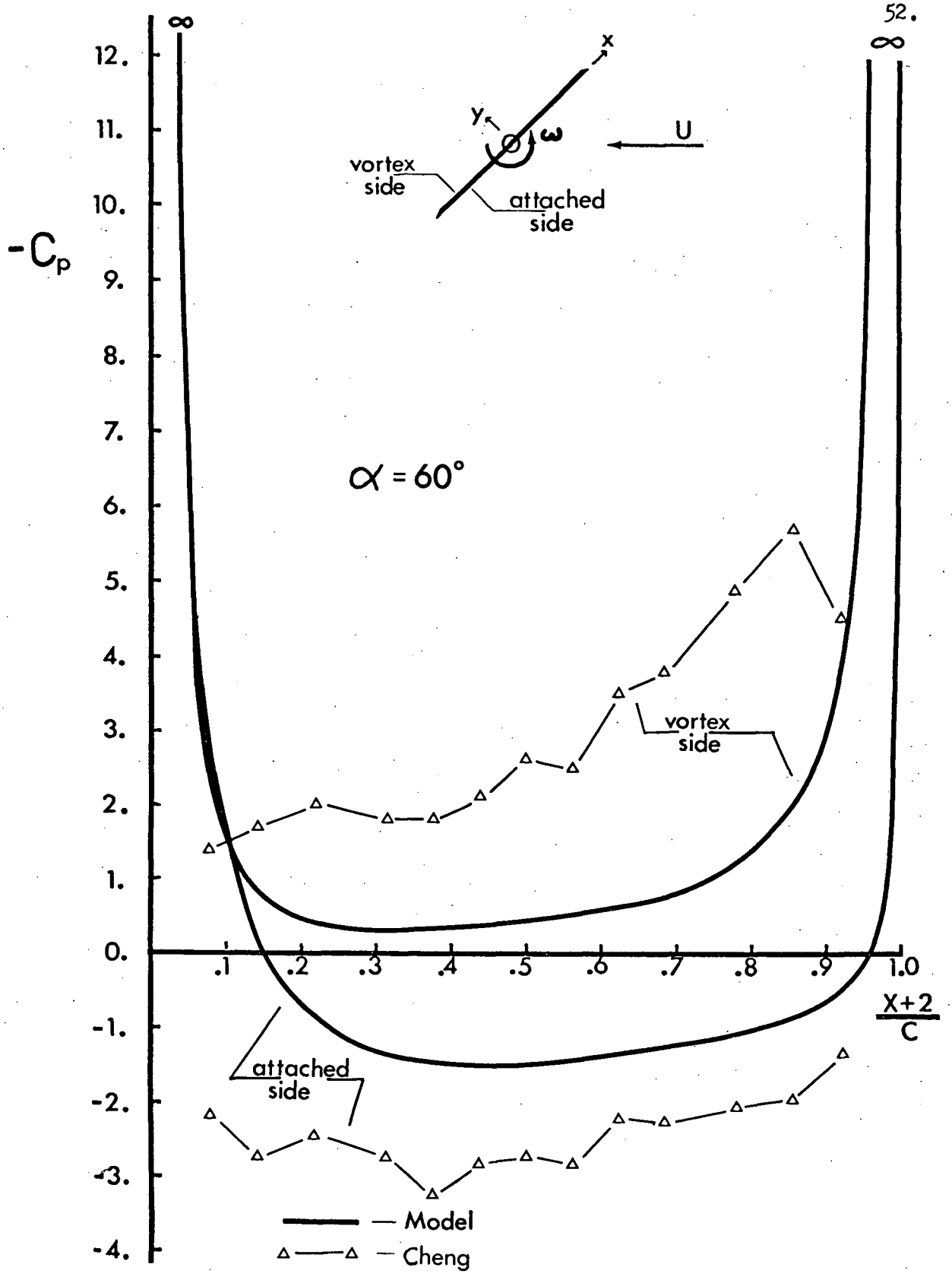

FIG. 27 PRESSURE COEFFICIENT - PLATE POSITION
ANGLE OF ATTACK = 60 DEGREES

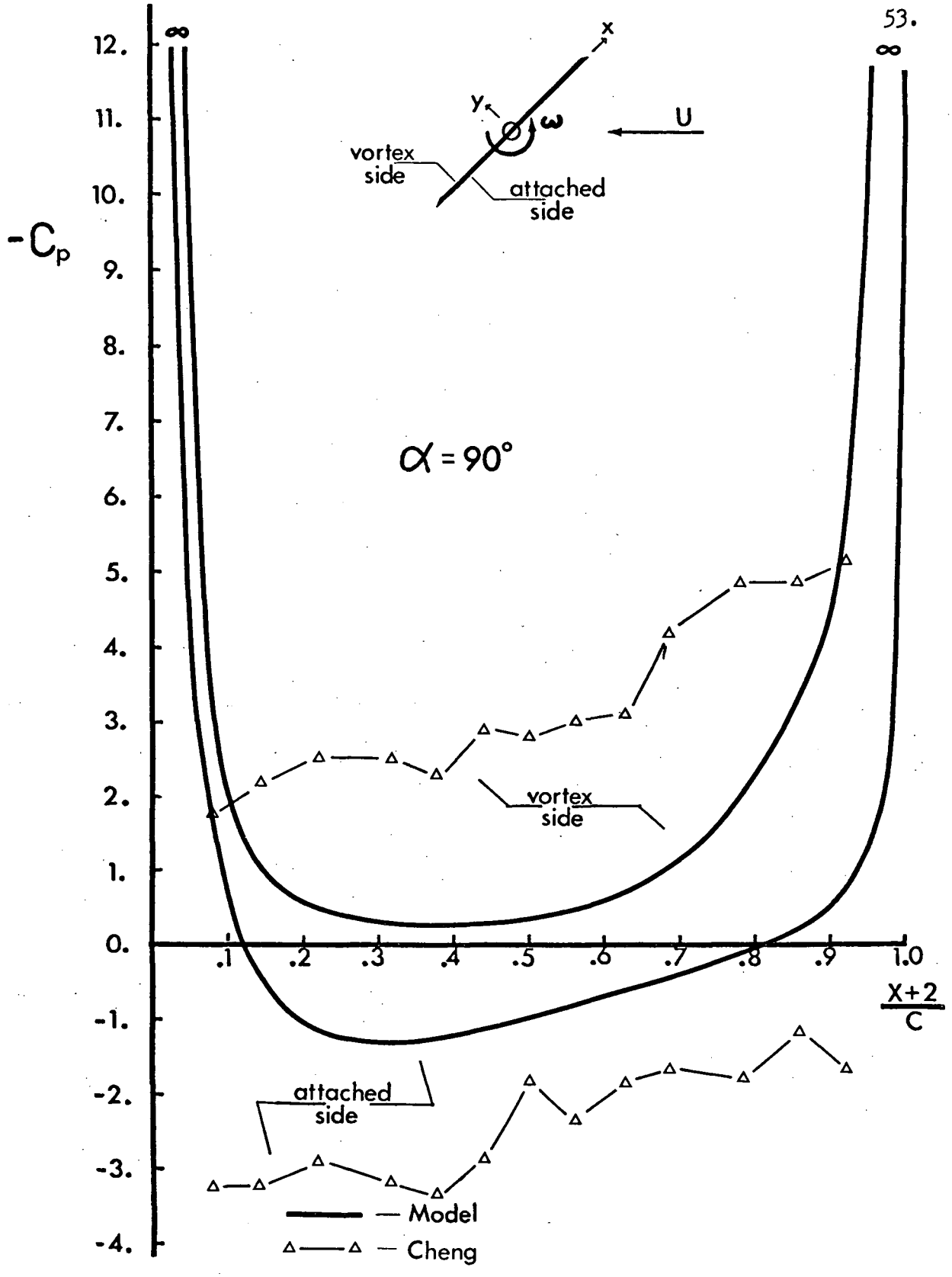

FIG. 28 PRESSURE COEFFICIENT - PLATE POSITION
ANGLE OF ATTACK = 90 DEGREES

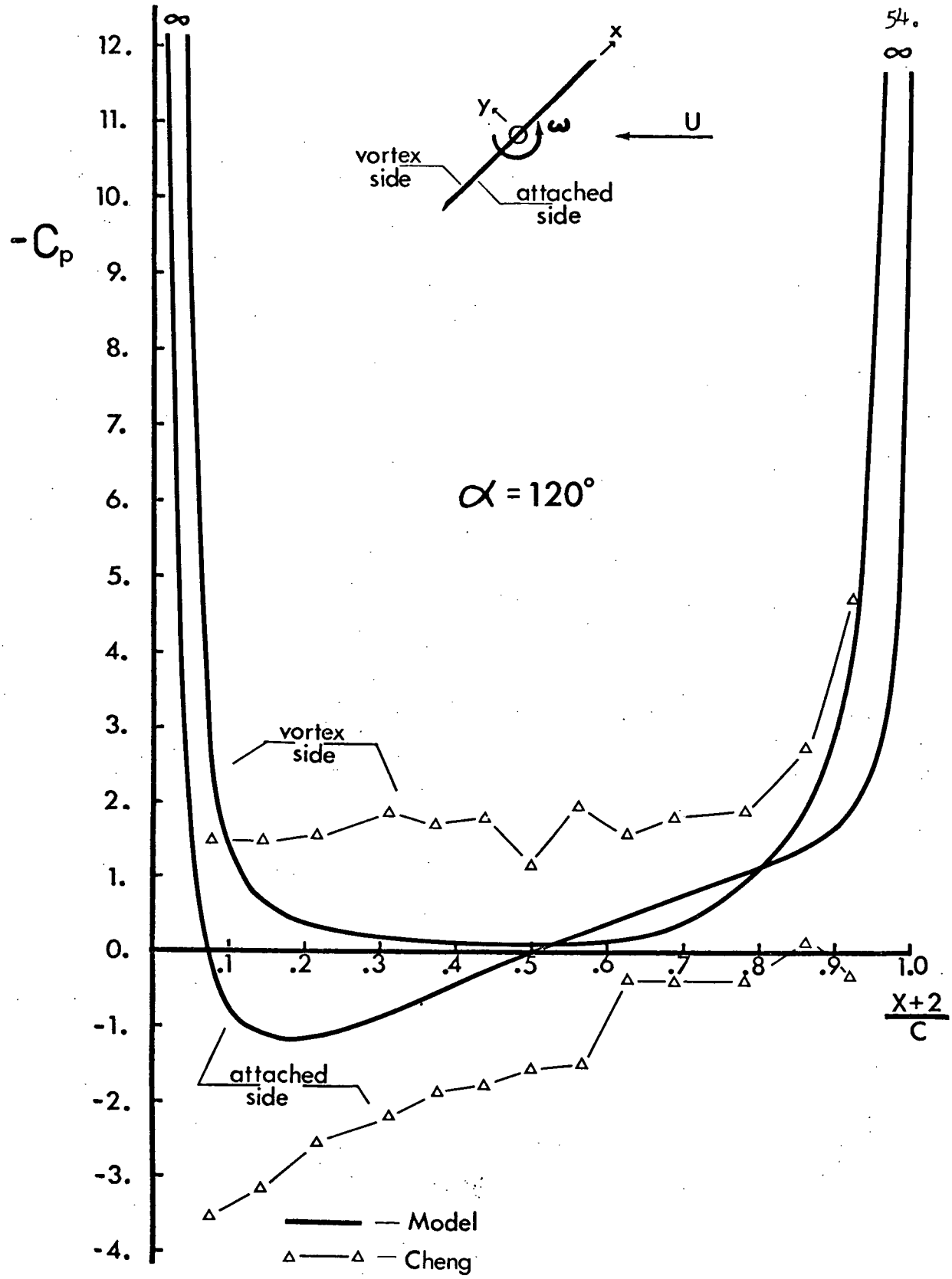

FIG. 29 PRESSURE COEFFICIENT - PLATE POSITION
ANGLE OF ATTACK = 120 DEGREES

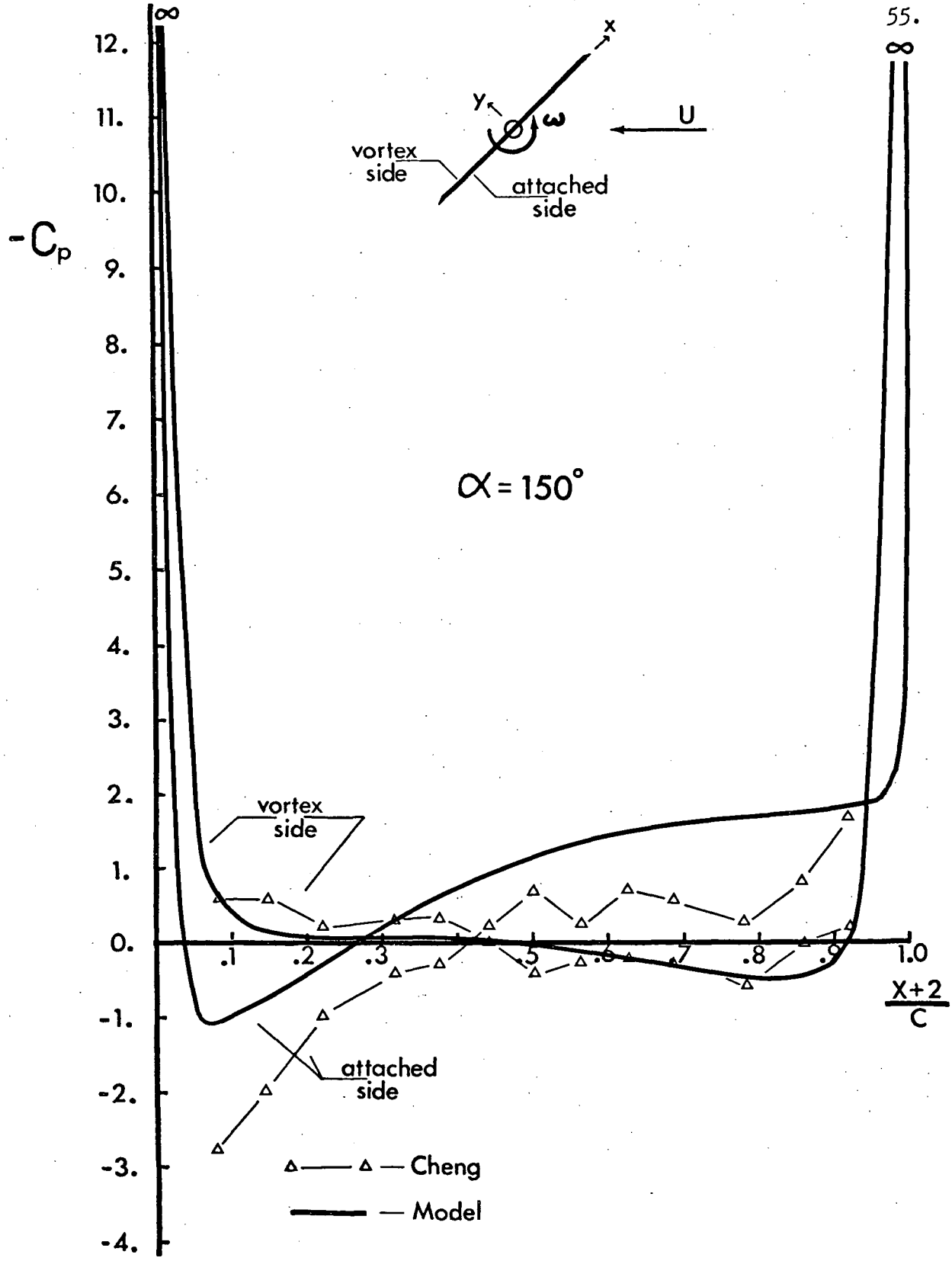

FIG. 30 PRESSURE COEFFICIENT - PLATE POSITION
ANGLE OF ATTACK = 150 DEGREES

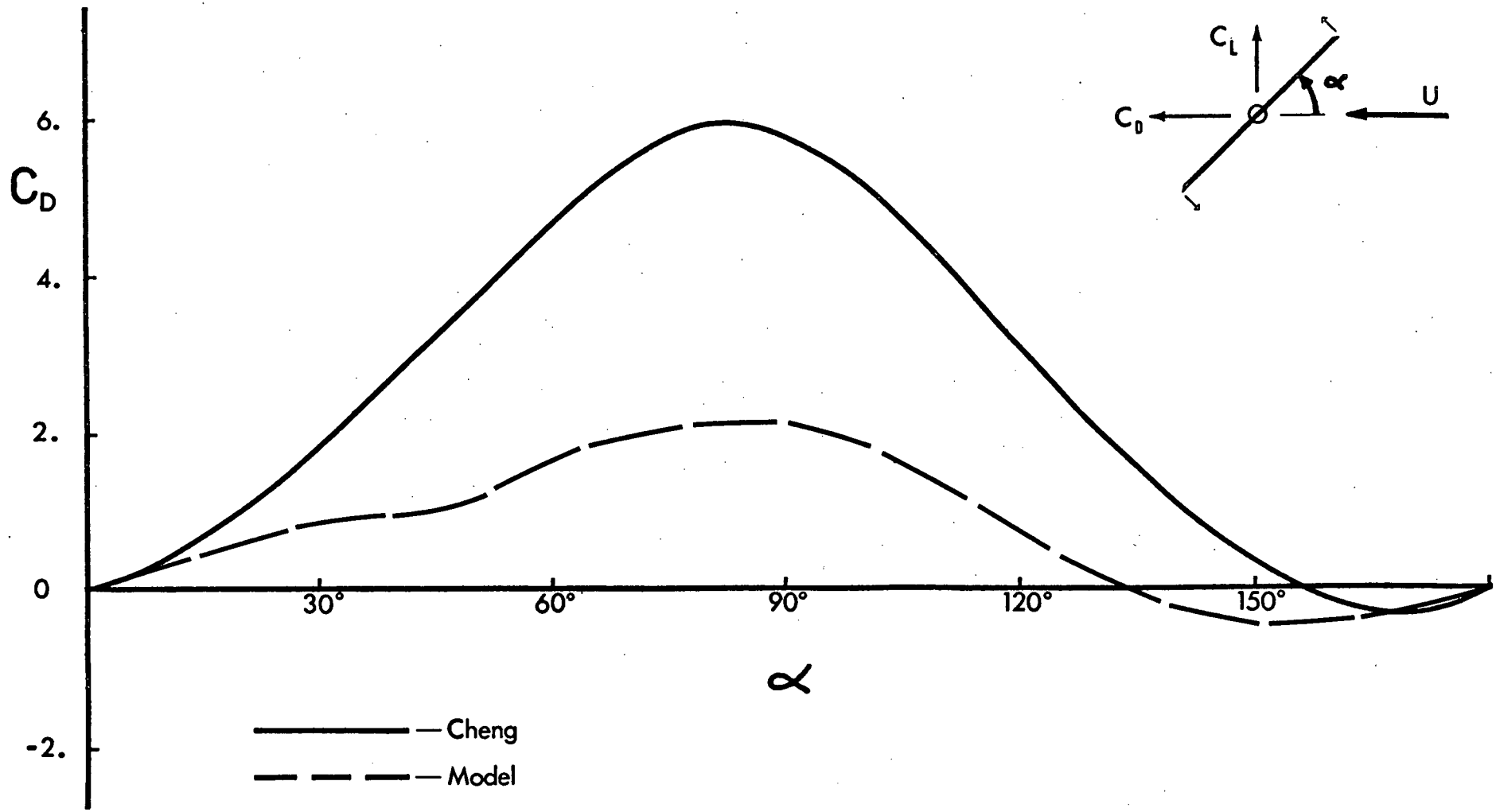

FIG. 31 DRAG COEFFICIENT - ANGLE OF ATTACK FOR MODEL AND CHENG'S RESULTS

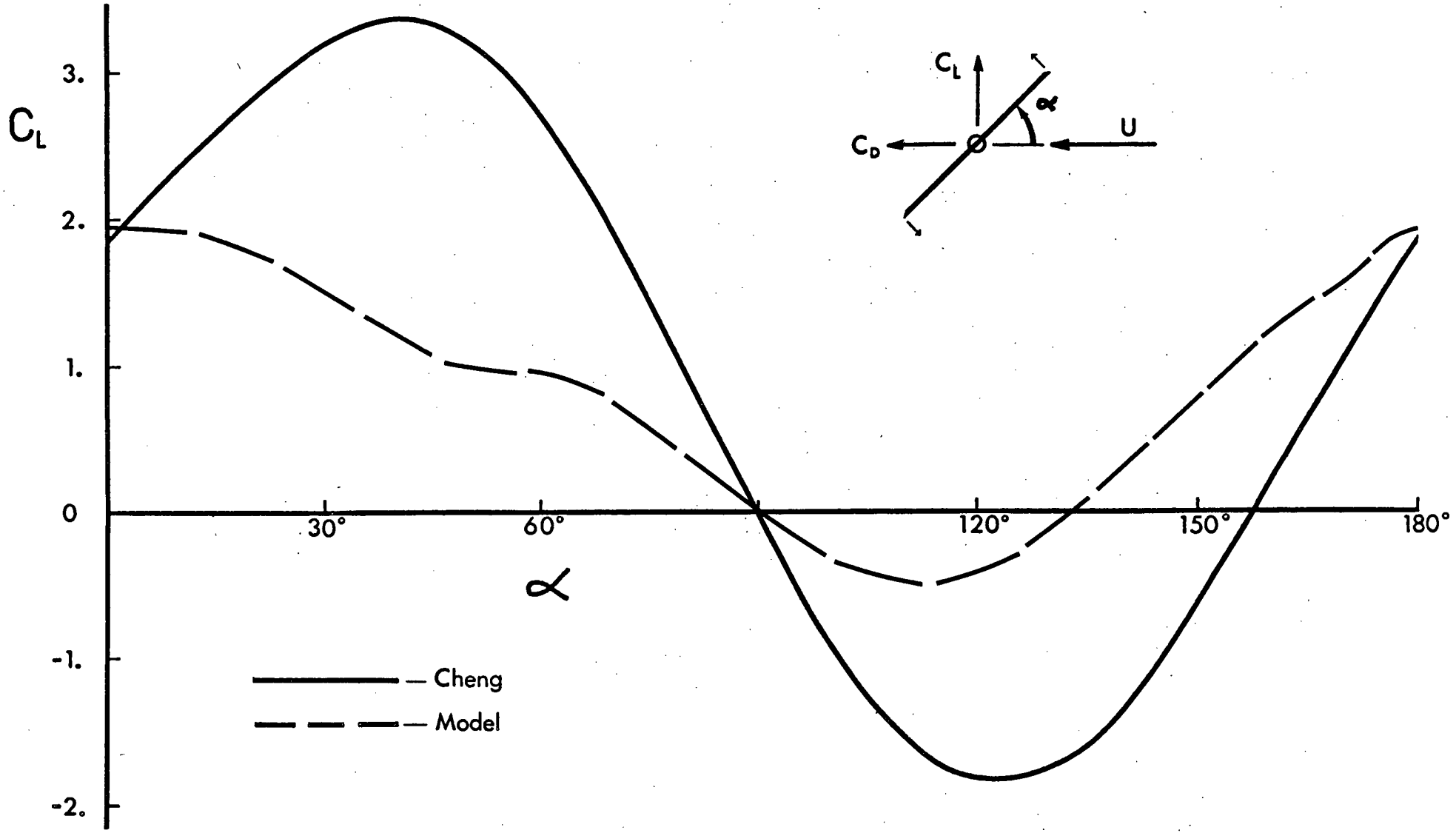

FIG. 32 LIFT COEFFICIENT - ANGLE OF ATTACK FOR MODEL AND CHENG'S RESULTS

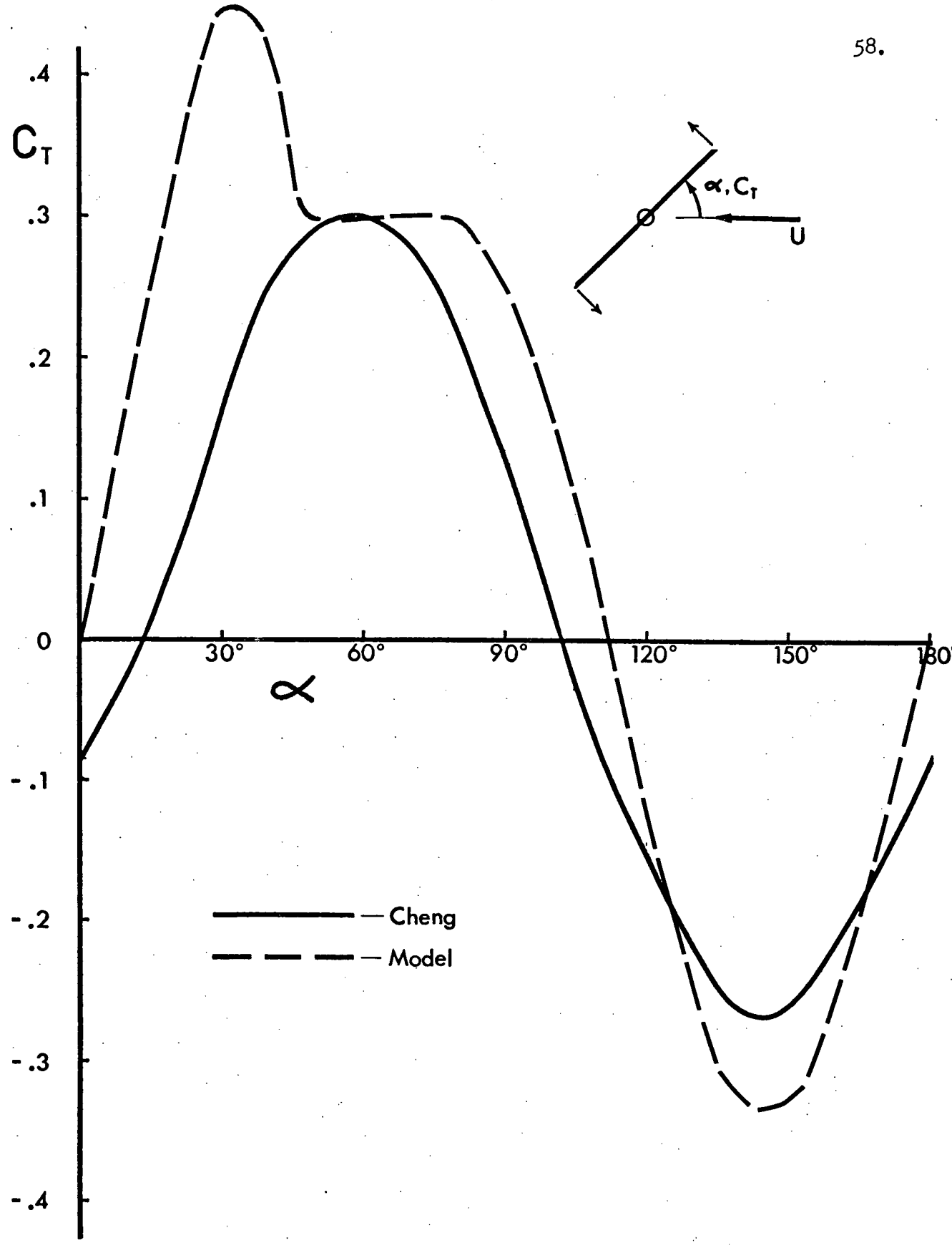

FIG. 33 TORQUE COEFFICIENT - ANGLE OF ATTACK FOR MODEL AND CHENG'S RESULTS

VI. SUMMARY OF RESULTS

Results of this project are summarized as follows.

1. The high suction peak near the upstream tip on the separated side of the plate is due to the formation of a large vortex at this tip every half-revolution.
2. Flow separation at the upstream tip at autorotational speed is delayed up to a positive angle of attack which is less than but near the relative zero angle of attack.
3. A vortex, which appears to be smaller than the vortex formed at the upstream tip, forms at the downstream tip.
4. The vortex shed from the upstream tip is the dominant feature of the downstream wake.
5. The wake undergoes angular deflection in the same direction as plate rotation for all angles of attack.
6. For the freestream range investigated, the tip velocity is linearly dependent upon the freestream velocity.
7. The angular velocity during autorotation is constant within experimental error.
8. The higher the freestream velocity, the lower the acceleration period to autorotation from start-up.
9. For the given assumptions of vortex position, vortex strength and the elimination factor ϵ, this model predicts the sign and trend of surface pressure for a cycle with reasonable accuracy. The magnitude of these curves, particularly at high angles of incidence, is not accurate.
10. The trend of the model drag coefficient versus angle of attack curve is accurate. The magnitude is not accurate for most of the cycle.

11. The model lift coefficient versus angle of attack is not very accurate in trend or magnitude. Maximum lift is predicted at zero degrees and it actually occurs at 45 degrees.

12. The model torque coefficient versus angle of attack is accurate in trend and magnitude, except for a spike at 30 degrees.

REFERENCES

1. Cheng, S. — "An Experimental Investigation of the Autorotation of a Flat Plate", M.A.Sc. Thesis, University of British Columbia, November, 1966.

2. Crabtree, L.F. — "The Rotating Flap as a High-Lift Device", Aeronautical Research Council Technical Report, Current Paper No. 480, 1960.

3. Neumark, S. — "Rotating Airfoils and Flaps", Journal of the Royal Aeronautical Society, January, 1963, pp. 47-61.

4. Claassen, L. — "Combined Free and Forced Convection from Horizontal Plates", M.A.Sc. Thesis, University of British Columbia, April, 1968.

5. HYCAM Manual — Model K30S1, Red Lake Labratories, Inc., 2971 Corvin Drive, Santa Clara, California, 95051.

6. Milne-Thomson, L.M. — "Theoretical Hydrodynamics", MacMillan, London, 1962, pp. 243-253, and pp. 154.

7. James, D.B.
Stone, J.W. — "The Characteristics of Thin Wings Autorotating About a Spanwise Axis", Department of Aeronautical Engineering, University of Bristol, Undergraduate Report No. 63, June, 1961.

8. Baird, H.
Pick, R. — "Autorotation of Flat Plates", Senior Year Project Report, Department of Mechanical Engineering, University of British Columbia, April, 1964.

9. Schlichting, H. — "Boundary Layer Theory", McGraw-Hill, New York, Fourth Edition, pp. 294-302.

10. Marks, L.S.
Baumeister, T. — "Standard Handbook for Mechanical Engineers", McGraw-Hill, New York, Seventh Edition, pp. 15-103.

APPENDIX

Since the air in the wake of the heated probe is at a higher temperature than the ambient conditions, the effect of buoyancy must be considered.

It can be neglected (9), if

$$N_r^2 \geq 10\, Gr$$

Considering the limiting case, then

$$Gr/N_r^2 = \frac{g(\rho_\infty - \rho)d}{\rho U^2} = .1$$

Solving, using the lowest freestream velocity (11.3 feet per second)

$$\rho = 4.9\,(10^{-6})\ slugs/ft^3$$

This corresponds to a much higher temperature than the maximum safe working temperature for Nichrome-V of 1,100 degrees Centigrade, according to reference 10.

It is interesting to note that the shear layers developed at the probe (Figs. 8-11) are not unsteady, even though the Reynolds number for the probe based on bulk conditions is greater than forty.

The power input to the probe was constant within the measurement error at 7.75 watts (2.5 volts r.m.s., 60 cycle) for the range of velocities (10-20 f.p.s.) in the experiment.